

INSTITUTE OF PHYSICAL CHEMISTRY,
POLISH ACADEMY OF SCIENCES

DOCTORAL THESIS

**Formation of chemical complexes at
subnanomolar concentration scale**

Author:

Krzysztof Aleksander
BIELEC

Supervisor:

Prof. dr hab. Robert
HOŁYST

*A thesis submitted in fulfillment of the requirements
for the degree of Doctor of Philosophy*

under

International Doctoral Studies of
the Institute of Physical Chemistry,
Polish Academy of Sciences

Kasprzaka 44/52
01-224 Warsaw, Poland



June, 2021

“Quidquid agis, prudenter agas et respice finem.”

“Whatever you do, do it wisely and consider the end.”

“Cokolwiek czynisz, rób to rozważnie i w spokoju oczekuj końca.”

Latin sentence

This work was supported by the National Science Centre, Poland, within the grant Maestro UMO-2016/22/A/ST4/00017.



Publications

 Google Scholar

 ORCID, 0000-0002-6023-5499

1. Bubak, G.; Kwapiszewska, K.; Kalwarczyk, T.; Bielec, K.; Andryszewski, T.; Iwan, M.; Bubak, S.; Hołyst, R. "Quantifying Nanoscale Viscosity and Structures of Living Cells Nucleus from Mobility Measurements" *The Journal of Physical Chemistry Letters* 2020, 12, 294–301.
2. Paczesny, J.; Bielec, K. "Application of Bacteriophages in Nanotechnology" *Nanomaterials* 2020, 10, 1944.
3. Zhou, Y.†; Bielec, K.†; Pasitsuparoad, P.; Holyst, R. "Single-molecule brightness analysis for the determination of anticancer drug interactions with DNA" *Analyst* 2020, 145, 6600–6606.
4. Bielec, K.; Bubak, G.; Kalwarczyk, T.; Holyst, R. "Analysis of Brightness of a Single Fluorophore for Quantitative Characterization of Biochemical Reactions" *The Journal of Physical Chemistry B* 2020, 124, 1941–1948.
5. Bielec, K.; Sozanski, K.; Seynen, M.; Dziekan, Z.; Ten Wolde, P. R.; Holyst, R. "Kinetics and equilibrium constants of oligonucleotides at low concentrations. Hybridization and melting study" *Physical Chemistry Chemical Physics* 2019, 21, 10798–10807.
6. Richter, Ł.; Bielec, K.; Leśniewski, A.; Łoś, M.; Paczesny, J.; Hołyst, R. "Dense layer of bacteriophages ordered in alternating electric field and immobilized by surface chemical modification as sensing element for bacteria detection" *ACS applied materials & interfaces* 2017, 9, 19622–19629.

Submitted:

7. Bielec, K.; Kowalski, A.; Bubak, G.; Kalwarczyk, T.; Holyst, R. "Ion complexation explains orders of magnitude changes in the equilibrium constant of biochemical reactions in buffers crowded by non-ionic compounds"

Patent applications:

8. Bielec, K.; Bubak, G.; Kalwarczyk, T.; Holyst, R. "Sposób wyznaczania stałych równowagi reakcji kompleksowania z wykorzystaniem pomiaru zmiany jasności molekularnej fluoroforu", (application number, P.432119)

Publications 4, 5, and 7 are parts of this dissertation.

Abstract

The formation of non-covalent complexes constitutes a majority of biochemical processes in living systems. The strength of the interaction in the formed complex – and its stability – is determined by its equilibrium constant (K). Several analytical techniques have been developed to quantify K . However, only fluorescence-based methods are sensitive enough to measure K in solutions of low concentrations (< 1 nM), in small volumes (< 1 μ L), and without immobilization of one of the reactants on the surface (as in e.g., microbalance technique or Surface Plasmon Resonance).

This Ph.D. thesis shows the discovery and development of a new fluorescence method to determine K . The method is based on observation of molecular brightness under change of local environment, further called "brightness analysis method". The Fluorescence Correlation Spectroscopy (FCS) determines the molecular brightness as the number of photons displayed by the molecules in time before and after the complex formation. Monitoring the change in photon counts enables the determination of the concentration of formed complexes in the system, hence the K . The obtained results were verified with the Fluorescence Resonance Energy Transfer (FRET) method.

Brightness analysis simplified the FRET analysis approach to operating **by using only one intrinsically fluorescent (or labeled) substrate** without losing its generality. As a model reaction of complex formation, I chose hybridization of complementary DNA oligonucleotides. The sensitivity of the method enabled us to determine the K for samples even at 80 pM. In such examples, the change of only 100 emitted photons (compared to the control sample) enabled us to analyse the result quantitatively. This improvement not only allows for **quick initial tests for determining the interaction of ligands with drugs or biomolecules** but also paves a way towards quantitative study of complex formation in living systems.

The experimental framework can be divided into three parts. The initial part studies kinetics and equilibrium constants of hybridization of oligonucleotides pairs by FRET analysis. This part determines the time after the equilibrium is being established in a wide range of concentrations of reagents (10

pM to 100 μM). Those experiments are followed by the determination of association, dissociation, and equilibrium constants at different conditions, i.e., temperature and ionic strength. The second part is directly related to the consequence of observing photophysical changes during the reaction, and development of the brightness analysis method. There, the theoretical basis was validated, as well as experimental factors influencing the measurement were determined. These results were specified and described in detail. Finally, the brightness variation study method was used to determine ion complexation by various molecular crowders.

Streszczenie

Reakcje tworzenia niekowalencyjnych kompleksów stanowią większość procesów biochemicznych w organizmach żywych. Siła oddziaływania w utworzonym kompleksie – a przez to, jego stabilność - wyznacza się za pomocą stałej równowagi (K). Szereg technik analitycznych umożliwia ilościowe określenie K . Jednak wyłącznie metody oparte na fluorescencji są wystarczająco czułe, aby zmierzyć K w roztworach o wyjątkowo niskich stężeniach ($<1 \text{ nM}$), w małych objętościach ($<1 \mu\text{L}$) i bez potrzeby immobilizacji jednego z reagentów na powierzchni (tak jak w np. przy zastosowaniu technik z użyciem mikrowagi czy powierzchniowego rezonansu plazmonowego).

Ta rozprawa doktorska rozprawa pokazuje odkrycie i rozwój nowej metody fluorescencyjnej do określania K . Metoda ta opiera się na obserwacji jasności molekularnej pod wpływem zmian lokalnego środowiska, zwana dalej „metodą analizy jasności”. Spektroskopia korelacji fluorescencyjnej (FCS) określa jasność molekularną jako liczbę fotonów wyświetlanych przez cząsteczki w czasie przed i po utworzeniu kompleksu. Monitorowanie zmiany liczby fotonów umożliwia określenie stężenia tworzonych kompleksów w układzie, a co za tym idzie, K . Uzyskane wyniki zweryfikowano metodą przenoszenia energii rezonansu fluorescencji (FRET).

Analiza jasności upraszcza podejście analizy FRET wykorzystując wyłącznie **tylko jeden fluorescencyjny (lub znakowany) substrat** bez utraty zalet pomiarowych techniki FRET. Jako modelową reakcję tworzenia kompleksu wybrałem hybrydyzację komplementarnych oligonukleotydów DNA. Czułość metody pozwoliła określić K dla przy stężeniu próbek równym 80 pM . W takich próbkach zmiana zaledwie 100 wyemitowanych fotonów (w porównaniu z próbką kontrolną) pozwoliła na ilościową analizę wyniku. To ulepszenie nie tylko pozwala na **szynkne wstępne testy do określania interakcji ligandów z lekami lub biomolekułami**, ale także otwiera drogę do ilościowego badania złożonego formowania się w żywych systemach.

Ramy eksperymentalne można podzielić na trzy części. Część wstępna bada kinetykę i stałe równowagi hybrydyzacji par oligonukleotydów metodą

analizy FRET. Ta część określa czas po jakim ustala się równowaga w szerokim zakresie stężeń odczynników (10 pM do 100 μ M). Wyniki te umożliwiły wyznaczenie stałych asocjacji, dysocjacji i równowagi w różnych warunkach tj. temperatura, siła jonowa. Druga część jest bezpośrednio związana z konsekwencjami obserwacji zmian fotofizycznych zachodzących podczas reakcji i rozwojem metody analizy jasności. Tu dokonano walidacji podstaw teoretycznych oraz wyznaczono eksperymentalne czynniki wpływające na pomiar. Wyniki te zostały sprecyzowane i szczegółowo opisane. Wreszcie, metoda badania zmienności jasności została wykorzystana do określenia kompleksowania jonów przez różne crowdery molekularne.

Contents

Abstract	vii
1 Introduction	1
1.1 Determination of the strength of interactions	4
1.2 Techniques for K determination	6
1.2.1 Fluorescence	6
1.2.2 Fluorescence microscopy	9
1.2.2.1 FCS	10
1.2.2.2 FRET	16
1.3 DNA and hybridization oligonucleotides	19
1.4 Interactions in crowded environment	23
2 Materials & Methods	25
2.1 Materials	25
2.1.1 Molecular crowders	25
2.1.2 DNA oligonucleotides	25
2.1.3 PB Buffer	28
2.2 Methods	28
2.2.1 Coverglass passivation	28
2.2.2 Emission spectra	29
2.2.3 Time-Correlated Single-Photon Counting setup	29
3 Results & Discussion	33
3.1 Equilibrium constant at subnanomolar concentration	33
3.1.1 Selection of analysis method	33
3.1.2 Single molecule experiments – surface adsorption	36
3.1.3 Apparent equilibrium constant	39

3.1.4	Approaching the equilibrium from either substrates or product side	43
3.1.5	Equilibrium constants, kinetics and activation energy . .	44
3.2	Brightness analysis method	47
3.2.1	Validation by FRET	50
3.2.2	Molecular brightness analysis of single labeled pairs . .	53
3.2.2.1	Experiments performed on double-labeled oligonucleotide pairs	54
3.2.3	Brightness analysis - Experimental errors	57
3.2.4	Sensitivity of molecular brightness analysis for single and double labeled pairs	59
3.3	Factors that affect K : crowded environment and ionic strength .	65
3.3.1	DNA Hybridization in crowded environment	66
3.3.2	Influence of ionic strength on DNA hybridization	68
3.3.3	Complexation of sodium ions by crowders	69
4	Summary and Conclusions	75
Bibliography		79

Chapter 1

Introduction

Therapeutic drug treatments target specific cell components (e.g., proteins, nucleic acids, etc.) [1–4]. In cells, the concentration of these targets occurs at the nano or subnanomolar level. For example, the number of copies of individual proteins per one Hela cell ($\sim 2600 \mu\text{m}^3$) is in the range from 10^7 down to 10^0 (single copies). Those numbers further varied within different compartments (e.g., cytosol and nucleosol) [5–7]. In one of my works, we showed that anthracycline drug-based anticancer therapy used in orders of magnitude times lower concentration than in medical treatments showed at least 100 times higher drug-target complex formation [8, 9]. These drugs have two parallel reaction mechanisms, the first being more effective at lower concentrations and the second (weaker) observed at high concentrations. The research of other drugs/therapies could provide more insights regarding their effectiveness of interactions at biochemical concentrations. Thus, how many compounds were rejected during screening tests but could be a good therapy at lower concentrations combined with an appropriate delivery method?

The discoveries of the last 30 years in the field of chemistry, biochemistry, biology as well as data science have provided much more excellent knowledge, and awareness in the design of new drugs or vaccines [10–13]. The global resources allocated to pharmaceutical companies' research and development department in only 2019 itself was 186 billion USD. The time and cost of implementing a single drug to the market is up to 20 years and amounts to an average of 2.6 billion USD [14–16]. The cost considers both the safety of patients (performing clinical tests) and the availability of drugs for a

broader spectrum of diseases. Traditionally, a novel drug can be obtained either by synthesizing an utterly new molecule or partially modifying the drug molecule currently available on the market [17]. The molecule obtained in this way was effective and generic. Hence it is also applicable to a larger group of patients. However, in the case of some diseases, current solutions do not provide effective treatment.

To address the needs of patients, the current trend, instead of synthesizing new molecular entities, focuses research on personalized biological product therapies, cell therapies, and gene therapies [18–20]. The development of these therapies makes it possible to cure diseases that were hopeless to heal in the past. Reducing the production batch to a few or even a single series causes that these therapies' price is often prohibitive [21]. Based on the most expensive drugs in the world in 2020, four are based on gene therapy, i.e., Zolgensma, Nusinersen, voretigene neparvovec glycerol phenylbutyrate [22–26].

Together with the emphasis on basic research, technological development made it possible to develop other new methods and therapies, which will make the current ones more affordable. Understanding the nature of the biochemical processes behind effective drug treatment is time consuming and complex. However, in the end, all interactions come down to simple types of reactions. To describe how pharmaceuticals work, it is enough to consider three different reaction types that can characterize most of our bodies' biochemical reactions. At the same time, the combination of those can describe complicated metabolic pathways.

- $A \rightarrow A^*$

This type of mechanism is directly related to the stability of a compound. The active state can be limited to various environmental conditions (e.g., pH or concentration of ions). This usually happens to the transformation of the molecular structure. Although, this reaction scheme can also be applied to conditions where component of the reaction, starts to be withdrawn from the reaction system (e.g., disposal of the reactant through the cell membranes or adsorption on the phase border).

- $A + B \rightarrow C$

The second type of reaction involves the reaction with the second component in the system (substrate) to create a third entity in the system, product C. These reactions are the basis of our body's biochemistry. During such reactions, substrates form strong chemical bonds, which create new molecules such as hormones, or utilize toxic metabolites, e.g., ethanol \rightarrow acetaldehyde. From a thermodynamic point of view, bonds created within product formation are irreversible (without additional agents or reaction components).

- $A + B \rightleftharpoons AB$

Lastly, most living systems' interactions are reversible, which means that two substrates form a temporary complex. The life time of the complex is mainly influenced by the strength of interaction between the substrates. The dynamic equilibrium is established in the system. After this time (dissociation of the complex), the substrates are still active and can still react with other molecules in the system. The concentrations of all reaction components are on the average constant. Although at the molecular level, the reaction still occurs in both directions. This type of interactions are common for all proteins, receptors, nucleic acids, fatty acids that build the membrane, etc.

Most known pharmaceuticals as well gene therapies are based on complex-forming reactions between the substrate (drug) and specific components of cells [8, 27]. The basis of these therapies being effective is understanding the mutual interaction of biomolecules in the cell, metabolic pathways, and editing or silencing gene information. Within the cell's interior, biomolecules appear in a small number of copies [7]. In most cases, the concentration of the molecules of interest is at the nanomolar scale or less. Over the past decades, the advancement of knowledge allowed us to track and locate single molecules' interactions at the cellular level [28].

These studies enable us to accurately describe a given biomolecule's reaction mechanisms (or compound) and observe its secondary interactions with other components in the system (the number of formed complexes and their stability). The direct observation of the movement and concentration created

tools for quantitative and temporal analysis of reactions directly in different cell compartments (i.e., predicting an efficacious concentration to produce the biological response and determination of the reaction equilibrium constant) [29, 30].

Therefore, to understand and thus design novel drugs or therapies, it is necessary to perform qualitative and quantitative analysis at a nanomolar concentration scale applicable in both *in-vitro* and *in-vivo*.

1.1 Determination of the strength of interactions

The strength of the formed bonds (interactions) can determine the assembled product's (or complex's) stability. In chemistry, the reaction's progress (i.e., $A + B \rightleftharpoons AB$) is observed as a result of averaging the interactions of all components in the system, but not just on a single pair of molecules [31–33]. The mean interactions of molecules ensemble are calculated using the two thermodynamic potentials: free enthalpy (H) and the Gibbs free energy (G). The determination of interaction at the molecular level does not include the important factor – the entropy (S), which considers the mutual configuration of all molecules in a given system. During any reaction, the energy of the system changes. Mutual relations between changes of ΔG , ΔH , and ΔS at a given temperature T is written as:

$$\Delta G = \Delta H - T\Delta S \quad (1.1)$$

After mixing the starting concentration of substrates, the reaction starts. As the reaction progresses, researchers want to know how many substrates reacted and formed the product. During the reaction, the concentration of formed products/complexes increases and stabilizes afterwards, see Figure 1.1. This means that reaction approached equilibrium state (at given conditions, concentration of complexes fluctuates over given value).

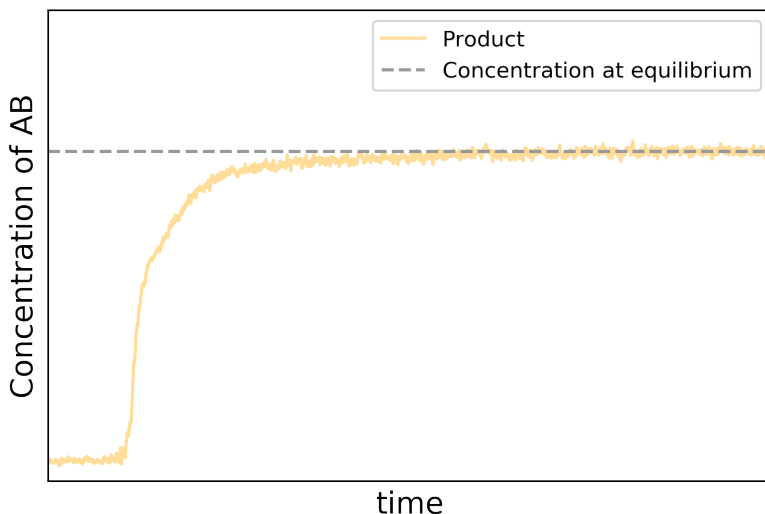


FIGURE 1.1: The formation of the non-covalent complex according to the $A + B \rightleftharpoons AB$. At the beginning in the reaction system only substrate A is present. After addition of the second substrate complex AB is formed.

Observed concentration fluctuation over values C_{AB}^{eq} means that there are still substrates in the reaction pool. The equilibrium constant K defines the ratio between a number of complex molecules and the rest of the substrates at an equilibrium state. Thermodynamically the K is directly related to the change of Gibbs free energy ΔG , and thus to the strength of interaction. The relation is written as:

$$\Delta G = -R \cdot T \cdot \ln(K) \quad K = \frac{k^+}{k^-} = \frac{c_{AB}^{eq}}{c_A^{eq} \cdot c_B^{eq}} \quad (1.2)$$

where R is the gas constant, c_A^{eq} , c_B^{eq} , and c_{AB}^{eq} are molar concentrations (at equilibrium) of substrates A, B, and complex AB, respectively. At equilibrium state, K is also defined as a ratio between association rate constant k^+ (how fast complex is formed) and dissociation rate constant k^- (how quickly the substrates separate). At given conditions (i.e., temperature, ionic strength, pressure, and pH), K value is constant. In aqueous solutions without any gaseous reagents, pressure may be negligible (as long as super high or low pressures are not involved).

1.2 Techniques for K determination

Investigation of reactions of formation of non-covalent complexes is essential for understanding and eventually controlling biochemical processes in living systems. The formation of complexes is ubiquitous in biological systems [34–36]. Significantly, most of the known pharmaceutical drugs are based on non-covalent interactions with specific enzymes or receptors [37–40]. Hence, more and more attention is paid to the tracking and quantitative analysis of biochemical reactions measured directly inside the living cell. The attention is drawn to the techniques that allow obtaining the result without the need to kill cells (e.g., homogenize them, cell lysates) and the sensitivity of detection way below the micromolar concentration scale. The equilibrium constant is determined by several analytical techniques. In the case of Isothermal Titration Calorimetry (ITC), Circular Dichroism (CD), and Nuclear Magnetic Resonance (NMR) the lowest concentration limit is about a few μM [41–43]. The samples of nanomolar concentrations can be characterized by Surface Plasmon Resonance (SPR) and Quartz Crystal Microbalance (QCM) [44–46].

However, those methods are robust in terms of experiment design. They require a long time of data collection, immobilization of a substrate on the detection surface, or do not allow for the collection of data directly from a given fragment of the cell. To avoid a large amount of substrates (aiming towards nanomolar concentration and below) and perform experiments now on the single living bacterial or eukaryotic cell (*in-vivo*), scientists shifted to fluorescence based techniques.

1.2.1 Fluorescence

Photoluminescence is the phenomenon of the emission of light radiation as a result of photon absorption, e.g., during irradiating a molecule with a laser [47]. A molecule capable of absorbing and emitting light radiation is called a fluorophore. As a result of photon absorption, the fluorophore goes into the excited state (transfers energy between its electronic states). Depending on the multiplicity of the excited state, photoluminescence is divided into fluorescence and phosphorescence. The diverse processes taking place in the excited state are presented using the Jabłoński diagram (see Figure 1.2), which

illustrates in a simplified way the distribution of energy levels and energy transfer between them. The excited fluorophore is out of the thermodynamic equilibrium. Hence the return to the ground state can occur in two ways of deactivation:

- Non-radiative – transition between two states without absorption or emission of photon (vibrational transition takes place). These transitions can occur between states of the same multiplicity, i.e. inside a given singlet or triplet state (the internal conversion) [48]. The non-radiative transition can also occur during the transition to a state with a different spin multiplicity (intersystem crossing).
- Radiative – transitions, as in the case of non-radiative transitions, can occur between states of equal spin multiplicities (e.g., excited singlet state and ground singlet state; $S_1 \rightarrow S_0$) are then called fluorescence or between states with different folds (e.g., excited triplet state and ground singlet state; $T_1 \rightarrow S_0$) called phosphorescence [49].

The differences between fluorescence and phosphorescence are experimentally observed in two ways: through the difference in energy of the emitted photons and the times, they occur (lifetime). During fluorescence emission, the electron (with spin \downarrow) in the exciting orbit is paired with a second electron in the ground state orbit but with the opposite spin (\uparrow ; spin-orbit coupling). This system's geometry causes electrons to strongly repel each other (higher difference in energy levels), causing higher energy emissions. Nevertheless, the transition is quick and usually takes a few nanoseconds. In the case of phosphorescence, the electron in the excited orbit (\uparrow) has the same spin orientation as the electron in the ground state (\uparrow). Parallel spin orientation of electrons at different orbitals results in lower energy levels (Hund's rule). Hund's rule forbids the process of changing the spin orientation, i.e., it occurs during the intersystem crossing with a low probability, and therefore, it is slow. The parallel geometry of electron spins and the intersystem crossing results that the phosphorescence may last from a few milliseconds to even tens of seconds.

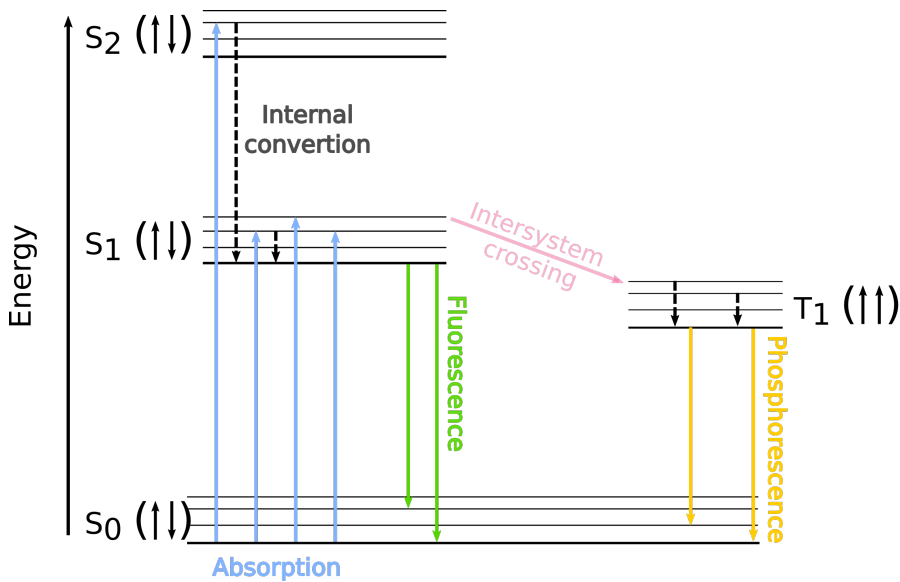


FIGURE 1.2: Exemplary Jabłoński diagram showing a photo-physical phenomena.

During the continuous excitation of the fluorophore, both fluorescence and phosphorescence may occur. The average photon emission intensity per molecule is called molecular brightness [50]. Under given experimental conditions, molecular brightness depends on many factors, such as the intensity of excitation, temperature, or solvent [8, 50, 51]. Those conditions also affect the ratio between photons emitted due to fluorescence or phosphorescence may be different.

Fluorescence is a common phenomenon in nature, both among living organisms (the presence of fluorescent proteins, e.g., Green fluorescent protein, GFP) and inanimate matter, e.g., rock minerals [52–54]. The development of technology allows observing the fluorescence signal of single photons at the time resolution reaching even the picosecond scale. Many experimental techniques use this phenomenon to track fluorescent markers in cells, determine structural elements of proteins, analyze reaction kinetics and the strength of intermolecular interactions.

1.2.2 Fluorescence microscopy

A combination of fluorescence and classical optical solutions created one of the essential tools used in life sciences - fluorescence microscopy [55]. The technique owes its popularity to the vast possibility of identifying and distinguishing (in terms of "color") subcellular structures while maintaining the resolution of traditional optical microscopy [56]. The widespread use of fluorescence microscopy is closely related to the development of new synthetic and naturally occurring fluorophores with known excitation and emission profiles and well-known biological targets. In biological research, the use of different fluorophores allows the identification and differentiation of cell-building components such as proteins and cell receptors, etc. Hence, the emphasis in the research is put on the development of fluorescent techniques that can be combined with super-resolution microscopy techniques (e.g., confocal microscopy, spinning disc microscopy, stimulated emission depletion (STED) microscopy, total internal reflection fluorescence (TIRF) microscopy, or scanning near-field optical microscopy (SNOM)) [57–60]. In practice, these techniques enable signal detection from a single molecule even from the area of several dozen nanometers. Additionally, by marking the probes with different dyes, several types of molecules are identified simultaneously.

The technique based on the simplest solution to increase the resolution is confocal microscopy [61, 62]. Fluorescence confocal microscopy makes it possible to control the depth of the measured area. This is due to eliminating the background signal from the focal plane, enabling the scan of selected space from a large sample in three dimensions. The key to the confocal approach is the use of a pinhole (or several pinholes), i.e., a confocal diaphragm with a small opening [63]. It eliminates the signal coming from the exciting cone's points outside of the focal plane (laser blur or light reflection), which effectively increases the resolution. Thus, by changing the focus within the sample (either by the movement of the objective lens or the microscope stage in the Z axis), it is possible to analyze the light coming from successive levels of the sample. In some microscope systems, the reduction of fluorescence emission signal by the pinhole, is followed by application of sensitive detectors (e.g., photomultipliers). An example of a confocal microscope operation scheme is

presented in the Figure 1.3.

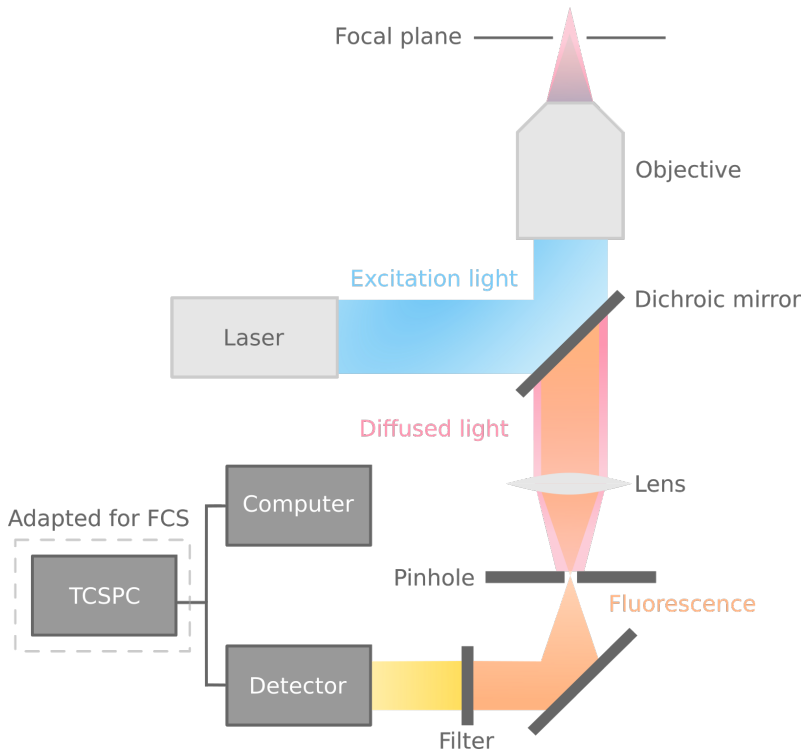


FIGURE 1.3: The confocal microscope consists of a light source (i.e., laser) that emits an excitation beam towards a dichroic mirror. The mirror acts as a filter allowing only light waves of a certain length to pass. Dichroic mirror reflects excitation beam towards internal mirrors to the microscope objective. The objective shapes and focuses the light beam within the sample. The sample's fluorescence is collected through the same optical pathway up to the dichroic mirror, which now passes through. The pinhole then filters the collected light beam by cutting out the signal from outside the confocal plane. Finally, the selected light waves go to the detector with a photomultiplier tube, where they are converted into a digital form.

1.2.2.1 FCS

Confocal microscopy allowed fluorescence techniques to reduce the observed volume significantly. Such reduction of the detection volume along with sensitive detectors (photomultiplier tubes or photon avalanche diodes) enabled to perform experiments at concentrations scale in which single molecules are observed within the confocal volume (nanomolar to picomolar) [64, 65]. Such

sensitivity of detection of fluorophores can accurately estimate the time of flight across the focal volume. Having precise knowledge of the size of the confocal volume and other experiment conditions (i.e., temperature and viscosity) enables to estimate diffusion coefficient of the fluorophore, and thus its hydrodynamic radius [66].

Confocal volume is sensitive to various factors such as optical alignment, optical saturation, and the changes in the refractive index of a biological sample [67]. The difference in refractive index for given objective and sample is more pronounced as the focal volume is more profound in the sample. Thus, the focal volume should be positioned just above the glass border ($<10\text{ }\mu\text{m}$) for such situations.

Correct calibration of the confocal optics is an important step in making measurements.

In fluorescence measurements using confocal techniques, the signal comes from the focus plane of the objective. Under these optical conditions, the observed volume is the ellipsoid extended along the optical axis. The detection volume is different from the ellipsoid volume and is in the order of femtoliters (e.g., $\sim 0.3\text{ fL}$ for 485 nm laser, 60x objective, 1.2 NA). As a result of the fluorophores' random diffusion movements, quantitative, time-dependent changes in the number of fluorophores in the confocal volume, called fluctuations, are observed.

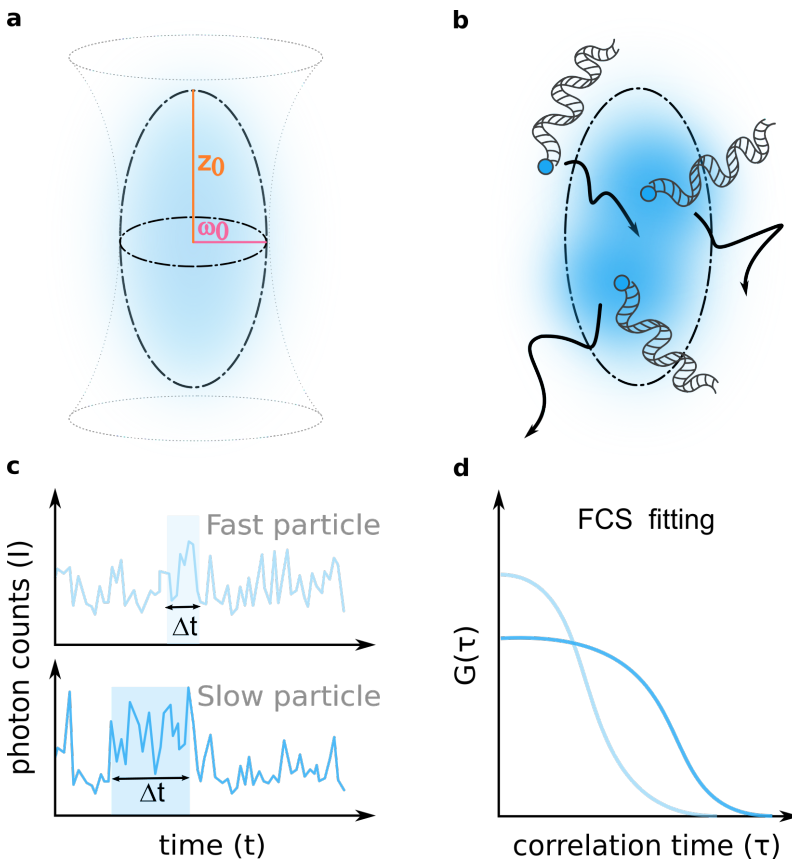


FIGURE 1.4: Principle of FCS theory. **a** Confocal volume is an ellipsoid. Limiting the volume with the use of the probability density function allows to calculate the effective detection volume with specific dimensions ω_0 and z_0 . **b** Fluorophores emitting photons only during diffusion across the confocal volume. **c** Photons collected from different samples present different fluorescence fluctuations intensity pattern. **d** The autocorrelation function enables transform intensity signal and present it as a plot of correlation magnitude to correlation time. Further analysis allows to determine the average sample concentration and diffusion coefficient.

During the measurements, the signal is mostly collected from effective detection volume, V_{eff} of long and short radii z_0 and ω_0 respectively, see Figure 1.4a. The ellipsoid-like volume size borders are defined by the probability density of the molecule detection, which is at least greater than $1/e^2$. Hence the detection volume is determined by:

$$V_{eff} = \pi^{\frac{3}{2}} \cdot \omega_0^2 \cdot z_0 \quad (1.3)$$

One of the fluorescence techniques that enable to measure the interactions at nanomolar scale and below is Fluorescence Correlation Spectroscopy (FCS) [68–70]. FCS's operational principle is based on the analysis of the temporal fluctuations in fluorescence intensity, using correlation analysis. In the case of experiments in aqueous solutions, changes in fluorescence intensity result from thermodynamic fluctuations - Brownian motion [71]. The signal from molecules is obtained only from a particular volume - i.e., a confocal volume, see Figure 1.4b. As a result of the fluorescence signal analysis, two pieces of information are obtained: the average number of particles within the volume (during a time of measurement) and the average diffusion time of flight across it. Once the shape and size of the confocal focus are known, it is possible to convert the average diffusion time through the detection volume into their average concentration and translational diffusion coefficient.

The data (in a simplified way) for FCS analysis of given fluorophore have to be stored as a single column of times when emission photon was recorded. This data is binned within a predefined time interval. After such operation, the data consist of two columns: binned time (t) and fluorescence intensity at time t , $I(t)$ (number of photons recorded within the single bin), see Figure 1.4c. Autocorrelation function of the fluctuation intensity $G(\tau)$ is the time average of the $I(t)$ and the intensity after the delay time $I(t + \tau)$:

$$G(\tau) = \langle I(t) \cdot I(t + \tau) \rangle = \int_0^t I(t) \cdot I(t + \tau) dt \quad (1.4)$$

The autocorrelation function normalizes the intensity fluctuations over time by the square of averaged fluorescence intensity. Thus, the form of autocorrelation function is presented also by using signal fluctuation intensity as a variances at time t from the mean value $\delta I(t) - \langle I(t) \rangle$:

$$G(\tau) = \frac{\langle I(t) \cdot I(t + \tau) \rangle}{\langle I(t) \rangle^2} - 1 = \frac{\langle \delta I(t) \cdot \delta I(t + \tau) \rangle}{\langle I(t) \rangle^2} \quad (1.5)$$

In terms of transnational Brownian diffusion the Equation 1.5 takes a different form. The autocorrelation function in such form is proportional to the probability function and is interpreted as follows. The correlation time $\tau = 0$ is the moment when any photon is observed (with the highest probability). As τ increases, the probability of observing another photon in τ time later

within the focal volume. The more as time passes, the probability of registering the photon is lower, where finally decreases down to 0 ($G(\tau) \rightarrow 0$), see Figure 1.4d. Thus, after complex mathematics the three dimensional diffusion **autocorrelation curve of a single fluorescent component** is presented as [47]:

$$G(\tau) = G(0) \cdot \left(1 + \frac{\tau}{\tau_D}\right)^{-1} \cdot \left(1 + \frac{\tau}{\kappa^2 \tau_D}\right)^{-\frac{1}{2}} \quad (1.6)$$

$$G(0) \approx \frac{1}{\langle N_p \rangle} \quad \kappa = \frac{z_0}{\omega_0} \quad \tau_D = \frac{\omega_0^2}{4D}$$

A given fluorophore diffuses by Brownian motion and can emit photons only inside a focal volume. The time the molecule diffuses through the focal volume (τ_D) is proportional to the mean traveled distance and its diffusion coefficient (D). A mean distance is proportional to the second power of the shorter dimension of the ellipsoid, ω_0^2 , see Figure 1.4a. Finally, Equation 1.6 enables to determine the average number of molecules (N_p) within the focal volume. Therefore, defined focal volume is required before performing FCS analysis. This is done by calibrating system with a dye of known diffusion coefficient. After this step, by FCS it is possible to determine the concentration of a given fluorophore and its diffusion coefficient.

Equation 1.6 takes into account only that the sample emits photons in the manner of fluorescence. The average fluorescence life time is in the order of nanoseconds, whereas the diffusion time for reference fast fluorophores i.e. Rhodamine 110 is order of tens of microseconds. This means that time for transition between singlet states is negligible in terms of fluorophore diffusion. However, when phosphorescence is observed, for most fluorophores or labeling dyes triplet lifetime, τ_T is in the order of microseconds. Thus, during flight across focal volume fluorophore that undergoes transition to triplet state may seem to be blinking (being dark for few μs). The contribution of average fraction of molecules that are in triplet state, T is added to the Equation 1.6 by additional exponential decaying function. The **autocorrelation curve for that includes triplet states** is given by:

$$G(\tau) = G(0) \cdot \left(1 + \frac{T}{1-T} \cdot e^{-\frac{\tau}{T}}\right) \cdot \left(1 + \frac{\tau}{\tau_D}\right)^{-1} \cdot \left(1 + \frac{\tau}{\kappa^2 \tau_D}\right)^{-\frac{1}{2}} \quad (1.7)$$

FCS in series of experiments, enables determining equilibrium constant and kinetics using a single component model. It is possible by determining the concentration of fluorophore. However, the reaction system has to be specific. One of the reaction components loses or gains fluorescent properties after complex formation in this system, but the change is binary; $0 \rightarrow 1$. Then the binding isotherm could be reproduced by monitoring the concentration of this component.

Equations 1.6 and 1.7 only take into account the presence of only one kind of fluorescent probe in the system. The FCS enables to analyse of the photon fluctuations from multiple fluorescent components. The **multi component representation of autocorrelation function** is considered a sum of fluorescent contributions (assuming that both particles possess equal molecular brightness).

$$G(\tau) = G(0) \cdot \sum_i^M \rho_i \cdot \left(1 + \frac{\tau}{\tau_{Di}}\right)^{-1} \cdot \left(1 + \frac{\tau}{\kappa^2 \tau_{Di}}\right)^{-\frac{1}{2}} \quad (1.8)$$

where, M is a number of components in the system and ρ is fractional contribution defined by $\sum_i^M \rho_i = 1$ and $\rho_i = \frac{N_i}{\sum_i^M N_i}$.

The last **correction for fact that fluorescent components have different molecular brightness**. There, fractional contribution calculated for multi component system has to be corrected. Such a case has been presented in the situation where there are only two components. If first component posses molecular brightness α and second component posses molecular brightness γ then observed fractional contribution ρ is corrected to physical fractional contribution, ρ^P as:

$$\frac{\rho_{P1}}{\rho_{P2}} = \left(\frac{\gamma}{\alpha}\right)^2 \cdot \frac{\rho_1}{\rho_2} \quad (1.9)$$

The equilibrium constant and kinetics of reaction $A + B \rightleftharpoons AB$ can be determined by FCS [30, 72]. It is required that the fluorescent substrate and the formed complex must be significantly different in terms of their diffusion coefficients (at least by the factor of two). By adding the known initial concentration of substrates, it is possible to determine the number of particles of each component at equilibrium state, and then equilibrium constant [73].

In multi component system analysis as many as possible variables (i.e., brightness, ρ_x , T_x , τ_{Tx} , and τ_{Dx}) should be extracted from isolated experiments and fixed during calculations.

1.2.2.2 FRET

Fluorescence resonance energy transfer, FRET is a phenomenon that enables to transfer of energy between two different fluorophores where only one can absorb a photon of this energy on its own [74–77]. In such a system of two chromophores (or more applicably – fluorescent tags) are named as follows, the fluorescent tag that absorbs energy is described as a donor, and it transfers energy in non-photonic way to the second fluorophore, the acceptor (of energy). To enable FRET, two requirements have to be met. First is the overlap of donor's emission and acceptor's absorption spectra. The second one is that both tags are located at a precisely tailored distance, see Figure 1.5.

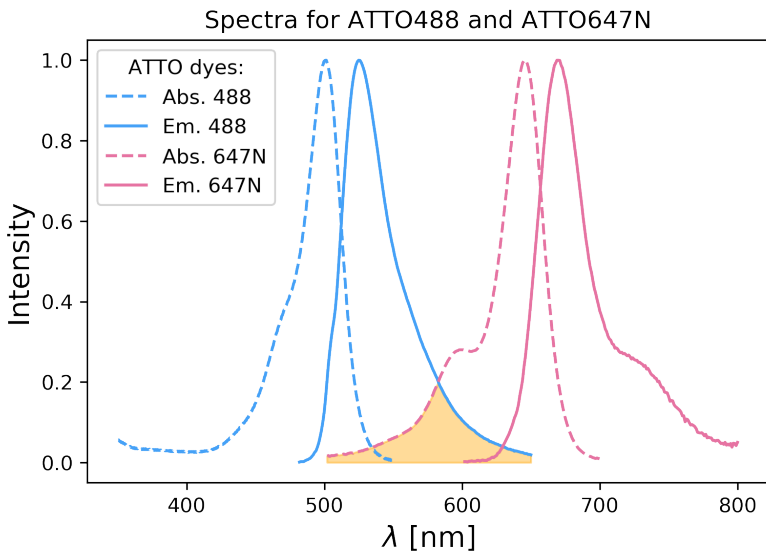


FIGURE 1.5: The example of FRET pair dyes where ATTO488 is a donor of energy and ATTO647N is acceptor. The FRET requirement of overlap of donor's emission and absorption of acceptor spectrum was filled with orange color.

FRET as an analytical technique may provide information such as: on whether the complex between reagents is formed, the strength of the interaction and to determine the distance between fluorophores. As an example, when a complex is formed, an excited donor fluorophore transfers the absorbed energy to a nearby acceptor fluorophore through a non-radiative manner long-range dipole-dipole interactions. Additionally, the orientation of transition dipoles of fluorophores influences the energy transfer efficiency [78]. For given pair of fluorophores used in FRET-based experiment, the most crucial parameter is Förster distance R_0 , which defines at which distance energy distance drops to 50% (usually up to 8 nm). R_0 is a function of:

$$R_0 \propto \kappa_D^2 \cdot q_D \cdot J(\lambda) \cdot n^{-4} \quad (1.10)$$

where, q_D is quantum yield of the donor chromophore, $J(\lambda)$ is spectral overlap of donor and acceptor spectra, κ_D^2 is directional orientation of transition dipoles, and n is refractive index of solvent/medium. For given formed complex with fixed distance r between donor and acceptor energy transfer efficiency is estimated as:

$$F_{eff} = \frac{R_0^6}{R_0^6 + r^6} \quad (1.11)$$

With known theoretical value of R_0 and distance r it is possible to determine how fast energy transfer occurs with the relation:

$$k_{FRET} = \frac{1}{\tau_{FD}} \cdot \left(\frac{R_0}{r} \right)^6 \quad (1.12)$$

where, τ_{FD} is a fluorescent lifetime of the donor. From the experimental point of view, only FRET combines the applicability at the subnanomolar level of substrates, nanoliter sample volume (enabling well-localized measurements), short time of data acquisition (of the order of seconds), and no particular requirements regarding substrate molecular dimensions, which makes it directly applicable to live cell studies of biochemical reactions [77, 79–81]. There are two approaches to quantify FRET using either intensity or fluorescence lifetime analysis. The fluorescence lifetime approach measures FRET efficiency via the magnitude of the decrease of donor fluorescence lifetime upon complex formation:

$$FRET_{eff} = 1 - \tau_{FD} / \tau_{FD0} \quad (1.13)$$

This analysis is very informative for determining the spatial structure of the complex, providing spatial resolution at the nanometer scale. However, when the equilibrium is not firmly shifted towards the product – which is often the case in the equilibrium constant measurements – the fluorescence lifetime histogram is a convolution of two overlapping exponential decays. Such overlap presents a challenge for data analysis related to proper separation of residual lifetimes originating from donor's, acceptor's molecules, and complex.

In the intensity approach, experiments are based on recording the changes in photons counts recorded in the donor and acceptor channels. When a complex is formed, the acceptor fluorescence signal appears at the cost of a decrease of the donor fluorescence. Considering this, the FRET efficiency is calculated as:

$$F_{eff} = \frac{I_{acc}}{I_{acc} + \eta \cdot I_{don}} \quad (1.14)$$

where, I_{acc} and I_{don} are background-corrected photon count rate values for the donor and acceptor channel, respectively. In the intensity analysis, the η is a system-dependent correction factor whose resultant value depends on two main factors. Firstly, it comprises emission quantum yields of the two dyes and collection efficiencies of the two channels with relation to the emission spectra of the dyes used. Secondly, it includes system construction characteristics that include applied features on the optical path, i.e., all dichroic mirrors, filters, and spectral sensitivity of the detectors [35, 82, 83].

The application of FRET in life sciences undeniably contributed to a deeper understanding and further investigating of biochemical and biophysical processes. The basic use of FRET provides nearly instantaneous qualitative result observed in the acceptor emission wavelength channel (change of the "color").

FRET enables to **determine complex formation, kinetics, and K** by the lifetime or intensity approach kinetics. It also enables **to determine structural properties at nanometer scale** without application of X-Ray based techniques (e.g., structure of proteins after binding to a receptor). Förster distance knowledge enables the calculation of the distance between molecules within the sample or formed complex. This utility of FRET is often referred to as the "**molecular ruler**".

1.3 DNA and hybridization oligonucleotides

Nucleic acid is one of the most important polymers on earth as it is a carrier of information in living organisms and viruses. A nucleic acid monomer's structural structure consists of a sugar moiety (ribose or deoxyribose), a nitrogenous base (cytosine; C, guanine; G, uracil; U, thymine; T and adenine; A), and a phosphate group. Nature distinguishes two nucleic acids: ribonucleic acid, RNA acid, and deoxyribonucleic acid, DNA. The difference between them is

not only due to the presence of specific sugar (ribose in RNA; deoxyribose in DNA) but also in nitrogenous bases, see Figure 1.6.

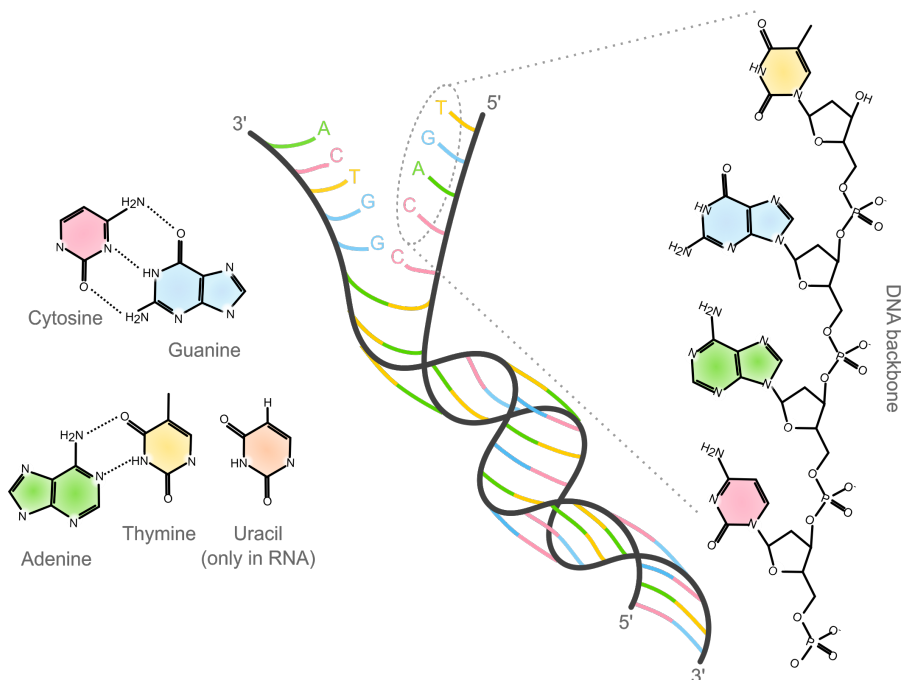


FIGURE 1.6: Scheme showing the formation of a DNA double helix, taking into account the most important elements of the notation and the chemical structure of the building base pairs.

Only four out of five bases are possible in DNA or RNA composition, with uracil only occurs in RNA and thymine only in DNA [84]. The three constituent elements (sugar, nitrogenous base, and phosphate group) of the nucleic acid monomer are bind by covalent bonds. As a whole, they are called simply the "base" as part of a long nucleic acid sequence. The single-stranded DNA chain is formed by linking the bases by covalent bonds between the phosphate groups. The DNA sequence is provided in notation from the beginning of the DNA backbone (called 5' end) until its end (called 3' end). The formation of double-stranded DNA (or RNA) is called hybridization and occurs between two single strands inappropriate configuration of the base building sequence. To create a double strand of DNA, two conditions must be met. First, the single base is paired only with a complementary one (G and C forms

triple hydrogen bonds, whereas A form a double hydrogen bond with either T or U). The second requirement is that sequences in those two strands have to be anti-parallel, which means that the one chain runs sequence from 5' to 3' but the other runs from 3' to 5'.

The hybridization of nucleic acids is one of the pivotal reactions of biochemistry. Binding between complementary nucleic acid strands underlies the replication of genetic information and its transcription to enable protein synthesis. In the case of long nucleotide chains *in vivo*, transitions between single- and double-stranded forms are usually enzyme-dependent and precisely controlled [85]. However, nucleotide pairing is also a crucial part of various procedures of molecular biology, including amplification of DNA sequences in a polymerase chain reaction (PCR), DNA sequencing, Southern and northern blotting, or gene expression monitoring [85–87]. Antisense therapies, based on binding oligonucleotides to mRNA, are emerging as a novel class of treatments for a range of conditions, including genetic disorders, cancer, and amyotrophic lateral sclerosis [88–91]. The use of DNA as a construction material for nanostructures, as in DNA origami, or as a sensing element in molecular beacons, opens a perspective of the application of DNA technology far beyond the field of molecular biology [92, 93].

All of the above examples of nucleic acid technology rely on spontaneous binding and unbinding of complementary strands. In most cases, the reaction concerns relatively short sequences, comprising between several and tens of nucleotides. For such oligonucleotides, strand pairing is a reversible process (duplex melting being the reverse reaction to hybridization) [94]. The strength of interactions between complementary strands is strongly dependent on the oligonucleotide sequence, temperature, and presence of ions in the solution [95, 96]. The increasing number of complementary base pairs between two oligonucleotide chains and the fraction of GC pairs raises the total gain in free Gibbs energy-related duplex formation, thus increasing interaction strength. Elevation of temperature destabilizes the duplex. Hybridization is also discouraged at low ionic strength conditions. Few cations stabilize the duplexes,

whose role is to screen repulsive electrostatic interactions between the negatively charged oligonucleotide backbones [97]. Despite these factors' apparently elementary nature, the overall process of oligonucleotide duplex formation and detachment is not trivial.

The DNA sequence is anti-parallel. Typically reading of a sequence starts from 5' to 3' end and should always be provided in this manner. For example, the 13 base pairs sequence is ATC GTG TAG GCA T then,



Thus, the complementary sequence is ATG CCT ACA CGA T.

An essential drive for research into the thermodynamics of oligonucleotide hybridization and melting was the popularization of PCR and the need for designing custom primers for this procedure. There are some easy-to-use tools available, such as, e.g., mfold or OligoCalc, that allow predicting the basic thermodynamic parameters for oligonucleotide pairing [98, 99]. The algorithms use the nearest neighbor model, which assumes that the total change in free energy upon forming a duplex is a sum of contributions of all base pairs [100, 101]. The free energy of each pair formation is influenced by the following base pair (nearest neighbor) due to stacking interactions. The calculations are based on empirical data [102, 103]. Empirical corrections for the presence of ions in the solution are also added [104]. However, these PCR-oriented procedures' main goal is to establish the melting temperature T_m (at which half of the strands are in a simplex form, and a half – in a duplex) with PCR primer design in mind. Therefore, they use simplified equations assuming an excess of one of the strands (primer) over the other (target DNA) and equality between the bound and free target DNA concentration due to the $T = T_m$ condition. Thermodynamic constants are only possible to predict for standard conditions, for which direct experimental reference for the nearest neighbor model parameters is available.

Kinetic studies of oligonucleotide hybridization and melting are even more scarce. There are several theoretical and simulation-based papers

proposing molecular mechanisms for the processes [105–108]. Melting of a duplex starts at the ends of the strand and proceeds along the chain; both one-sided and two-sided melting models seem feasible [107]. Hybridization is expected to occur analogously, with the formation of an initial contact (2–3 base pairs) followed by either dissolution of such pre-complex or full-duplex formation via a zipper mechanism. Binding may be hindered by the limited diffusional and conformational freedom of the strands after immobilizing one of them on a surface [109]. Possible secondary structures of strands are also known to slow down the kinetics of duplex formation [110, 111]. Thermodynamics and kinetics of formation of secondary structures such as hairpins constitute a critical issue intimately related to hybridization [112–115]. Kinetic aspects of strand pairing are also crucial for the design of DNA-based functional materials utilizing strand displacements and optimization of PCR processes [107, 116].

1.4 Interactions in crowded environment

Biochemical reactions take place in a complex system which is the smallest structural and functional unit of living organisms - a cell [30, 34–36, 117]. Regardless of whether it is a bacterial, plant, or eukaryotic cell, the interior is occupied by a high concentration of macromolecules and structural elements. The cell interior can also compartmentalize it for individual organelles. For example, in eukaryotic cells, even more than 60% of the cell's volume may be occupied by cytoskeletal elements (i.e., microtubules, filaments, microfilaments) and cellular organelles (i.e., nucleus, mitochondria, endoplasmic reticulum, Golgi apparatus, endosomes, lysosomes, peroxisomes, etc.). Additional contribution (30% on average) to space occupation are biomacromolecules, particles, and ions suspended in the cytoplasm. Accumulated molecules in a small volume of the cell interact with each other throughout all types of intermolecular types of interactions. This highly crowded environment affects physical parameters such as diffusion coefficients, structures of molecules, and strength of interactions. In literature, this phenomenon is called the molecular crowding effect.

Molecular crowding in cells is one of the critical parameters affecting the rates and equilibrium of biochemical reactions compared with those observed in the systems without additional cosolutes. Molecular crowding adds two additional interactions to the system. First is the repulsion due to interaction with the crowder's core (excluding volume resulting from the impossibility of occupying the same position in space). Second is a long-range attraction due to the presence of different chemical moiety (or presence of charges) in the crowder structure [118]. The presence of these additional interactions allows some proteins to adopt a specific structure that is much less stable in an uncrowded environment [119, 120]. It was observed that crowders in *in-vitro* experiments could also affect the formation of the complexes (shifting reaction either forward or backward) [121, 122]. For example, inert crowders could slow down (and eventually stop) the Kinesin-1 driven transport along microtubule [123]. Although when crowders are bigger than substrates molecules, a particle's motion is primarily the same as in a non-crowded environment [124, 125].

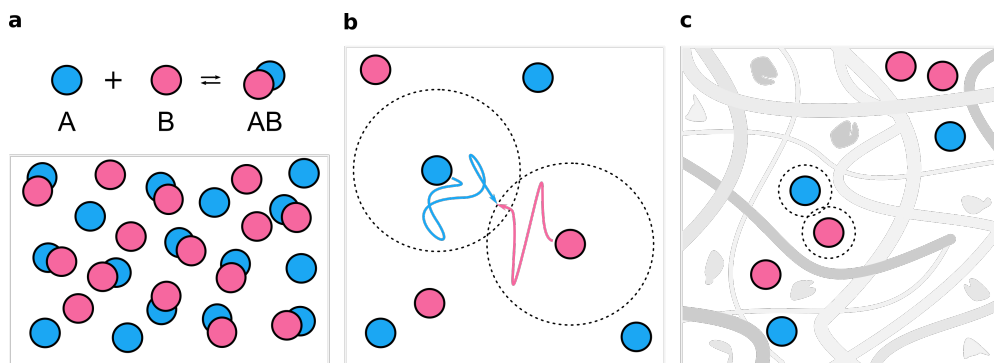


FIGURE 1.7: **a** Formation of non-covalent complexes in bulk solution is a mixture of constantly reacting substrates and formed complexes. **b** In non-crowded environment reactions are limited only to the diffusion of molecules and thermodynamic parameters of the system. **c** In crowded systems the diffusion of molecules is obstructed by crowded environment. Its presence excludes reactive volume available for molecules.

Chapter 2

Materials & Methods

2.1 Materials

2.1.1 Molecular crowders

Cosolutes such as Dextran 40k and Dextran 70k biosynthesized by the non-pathogenic organism *Leuconostoc*, Ficoll 400 and Poly-ethylene glycol (PEG) 400 were purchased from MilliporeSigma , Germany. Both ethylene glycol and glycerol 99.5 wt.% were bought from Chempur, Poland.

2.1.2 DNA oligonucleotides

All oligonucleotides were purchased from IBA GmbH, Germany. The strands were custom synthesized and labeled with Atto dyes at either 5' or 3' ends – see Figure 2.1 for sequences and labeling information. The sequences were designed in such a manner that no hairpin formation or alternative binding could occur. Oligonucleotides were purified by the manufacturer using the IBA Premium PAGE method and lyophilized. Upon reception, the strands were resuspended in Tris EDTA (TE buffer, 10 mM Tris, 1 mM EDTA pH=8) to obtain a stock of concentration of 100 µM, aliquoted and stored at -20°C. No additional purification was applied afterward. Experimental concentrations of oligonucleotides were obtained by diluting stock solutions in Phosphate Buffer (PB), pH=7.4 (the concentration of buffer is mentioned *explicite* before described experiment). Mixtures of complementary strands were incubated at 25°C. The incubation time depends on the sample concentrations - the lower

concentration, the longer the incubation time. The details are described further in *Results and Discussion* chapter.

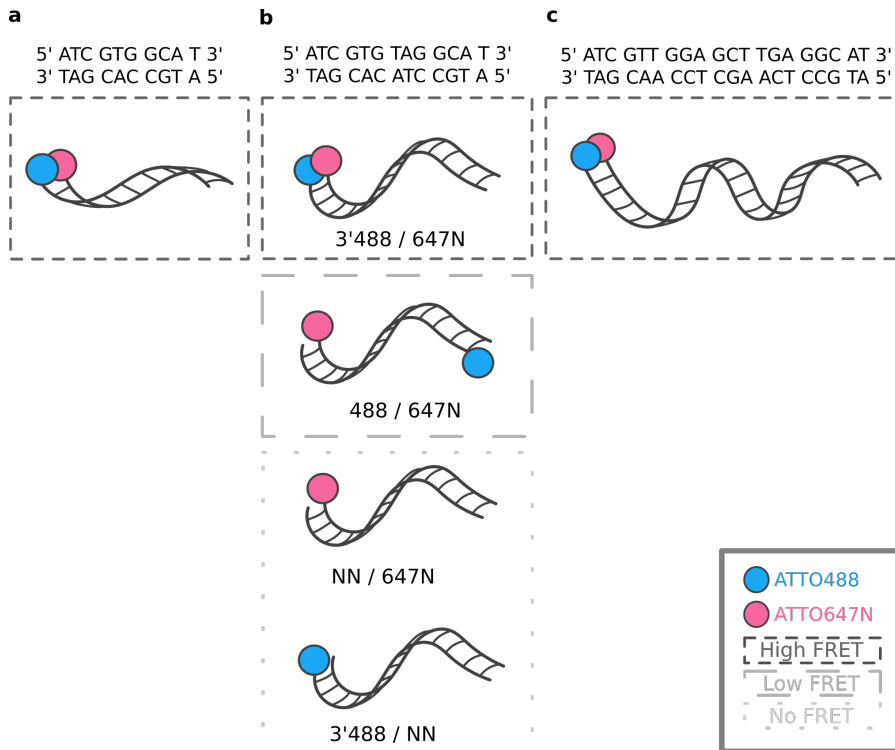


FIGURE 2.1: Oligonucleotides used in the experimental part of this study, together with the fluorescent dyes, base sequences, and an overview of the FRET energy transfer efficiency.

Photo-damaging of labeling dyes was prevented by two factors: 1) No single dye was directly irradiated for a prolonged time (as it is a case in most imaging-based experiments), due to the fast diffusion of the probes ($D > 120 \mu\text{m}^2/\text{s}$). 2) The dyes, on average, were illuminated by $50 \mu\text{W}$ (laser power measured before entering the objective) over time $t_D = 64 \mu\text{s}$, the time of diffusion across a focal volume. One of the main factors which affect the molecular brightness of fluorophore is excitation laser power (LP). The most comparable laser power measurement method is to set the photodiode sensor at the end of optical path-way. The measured value is considered as the total amount of photons excited by the sample. Setting the LP is crucial not only for our measurements but also for the biological samples. For biological

samples, it is preferable to use the lowest possible power where samples can still obtain a sufficiently high SN ratio. This reduces issues like photodamage and phototoxicity. Therefore to choose optimal laser power, a series of photon count rates were acquired for single-strand oligonucleotides labeled both with ATTO488 and ATTO647N at different laser power levels. The photon time trace was stable at each point which lies on a linear region of function presented in Figure 2.2. Therefore to obtain a sufficiently high SN ratio, the laser power was chosen before the inflection point. The observation of inflection points gives information about relative photobleaching and indicates the region at which detectors start to saturates (nonlinear response).

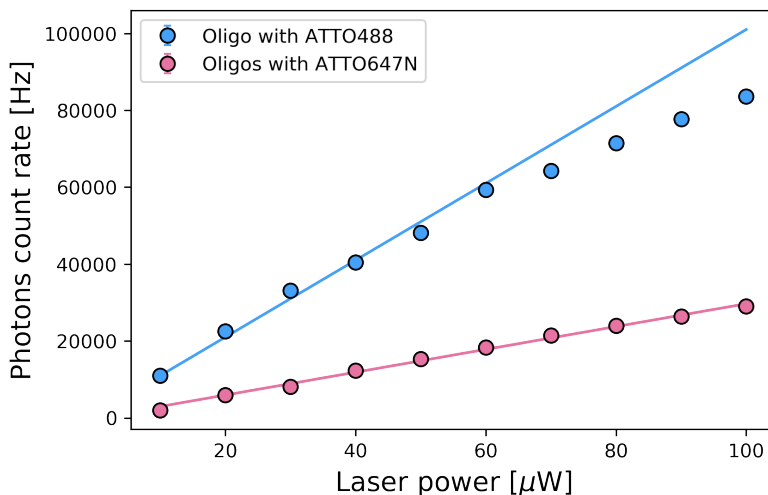


FIGURE 2.2: Series of photon count rate measurements for oligonucleotides labeled with either ATTO488 or ATTO647N of 2 nM concentration. The lines represent the trend line of expected photon counts per second fitted for the linear region < 50 μW and extrapolated.

In additional tests performed at laser power and observation time higher than in the standard protocol, we observed no photobleaching. Experiments were performed to ensure quality control using FCS and FRET. In FCS, auto-correlation curves fitted the single-component free diffusion model very well and the obtained hydrodynamic radii matched the values expected for the labeled oligonucleotides. These two results combined confirmed no perceptible amounts of free dyes in the solutions nor unlabeled DNA strands.

2.1.3 PB Buffer

The phosphate buffer is based on the use of two solutions of sodium dihydrogen phosphate, NaH_2PO_4 (solution X) and sodium hydrogen phosphate, Na_2HPO_4 (solution Y). Both solutions were prepared at a concentration of 200 mM. Then, to obtain the desired pH, solutions were mixed in v/v ratio. The experimental buffer was set to $\text{pH} = 7.4$ (marked bold), according to Table 2.1. To obtain 100 mM buffer, after mixing the X and Y solutions, 100 mL of MiliQ water was added to the final solution.

TABLE 2.1: PB buffer recipe. Experimental composition was marked in bold, unless stated otherwise.

pH	X [mL]	Y [mL]	pH	X [mL]	Y [mL]
5.7	93.5	6.5	⋮	⋮	⋮
5.8	92.0	8.0	6.9	45.0	55.0
5.9	90.0	10.0	7.0	39.0	61.0
6.0	87.7	12.3	7.1	33.0	67.0
6.1	85.0	15.0	7.2	28.0	72.0
6.2	81.5	18.5	7.3	23.0	77.0
6.3	77.5	22.5	7.4	19.0	81.0
6.4	73.5	26.5	7.5	16.0	84.0
6.5	68.5	31.5	7.6	13.0	87.0
6.6	62.5	37.5	7.7	10.5	89.5
6.7	56.5	43.5	7.8	8.5	91.5
6.8	51.0	49.0	7.9	7.0	93.0
⋮	⋮	⋮	8.0	5.3	94.7

2.2 Methods

2.2.1 Coverglass passivation

The procedure for coverglass passivation was based on a published standard protocol [126]. Briefly, #1 lime glass coverslips were extensively cleaned with

deionized water, acetone, and 1M potassium hydroxide. Then, piranha etching and aminosilanization using (3-Aminopropyl)triethoxysilane (APTES) in methanol were performed. Finally, N-Hydroxysuccinimide (NHS) ester of PEG (5 kDa) was coupled to the amine groups, forming a uniform PEG layer on the glass surface. Cover glasses used for the procedure were manufactured by Menzel Gläser. All chemicals used were obtained from Sigma Aldrich/Merck.

2.2.2 Emission spectra

The emissions spectra of labeled oligonucleotides were recorded by spectrophotometer (Agilent, model: Cary Eclipse, excitation wavelength: 480 and 630 nm at 25°C.

2.2.3 Time-Correlated Single-Photon Counting setup

Measurements were performed using an inverted confocal microscope Nikon EZ-C1 setup equipped with a water immersion Nikon PlanApo 60x objective (NA = 1.2). A triple band-pass filter (485 / 561 / 635 nm) by Chroma (USA) guided light through the objective.

The sensitivity of the system together with time filtration of the signal was obtained by equipping the confocal unit with a PicoQuant LSM system that includes PicoHarp 300 Time-Correlated Single Photon Counting (TCSPC) module and two Single Photon Avalanche photoDiodes (SPAD) PerkinElmer Optoelectronics and Micro Photon Devices (Milan, Italy). Wavelength filters and dichroic mirrors placed in front of the detector were manufactured by Chroma (USA). Two pulsed diode lasers 485 and 636 nm (PicoQuant GmbH, Germany) were used as excitation light. Lasers pulses were controlled by the Sepia II laser controller (PicoQuant GmbH) and the SymPhoTime 64 software.

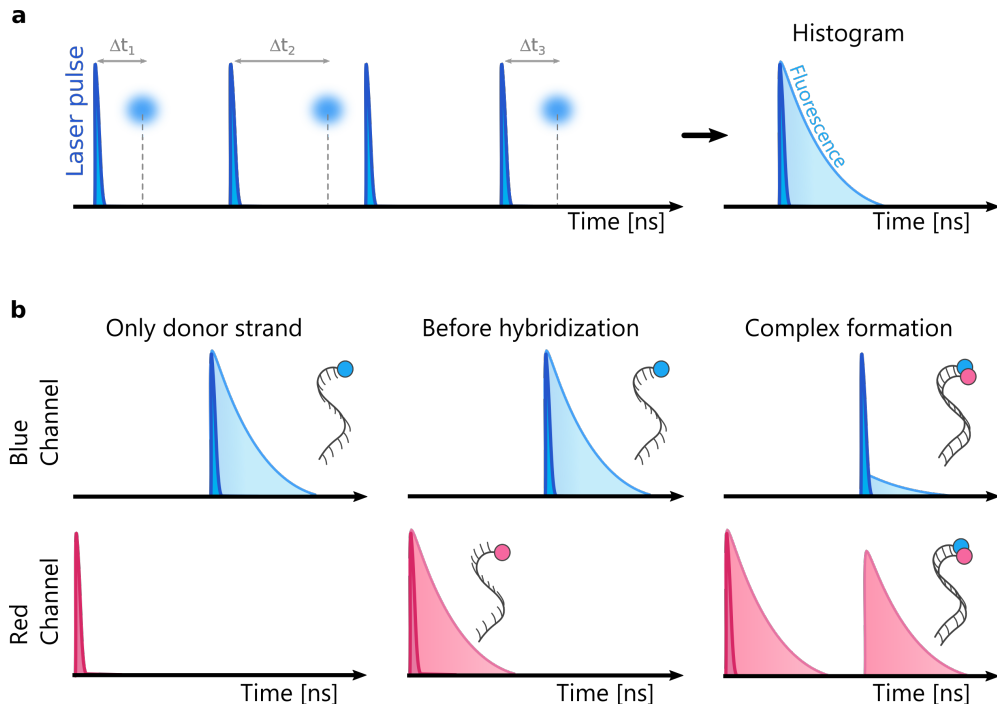


FIGURE 2.3: The scheme of data acquisition and analysis using pulsed interval excitation and Time-Correlated Single Photon Counting. **a** The TCSPC system records two regimes of time: from the start of the measurement and after each laser pulse. The recorded photon data can be presented as a histogram of emitted photons in the function of the time after the laser pulse. The histogram represents the probability of recording photons after excitation, which can be understood as a fluorescence lifetime decay function. **b** Using two intervalled excitation lasers enables to distinguish the emitted photon by specific time gate and the color of a channel. For a sample with only the ATTO488-labeled strand, after the blue pulse, the photons are observed only in the blue channel, whereas after the red pulse only Instrument Response Function (IRF) is recorded. When a duplex is formed, the donor (ATTO488) energy is absorbed after a blue laser pulse is transferred to the acceptor (ATTO647N), and fluorescence is observed in the red channel instead of the blue.

The pulse laser combined with single-photon counting overtime enables to record two regimes of time when a single photon was recorded. The first time took into account when the photon reached the detector from the beginning of the experiment. The second time gives the value that has passed since the last laser pulse. Due to high frequency of the laser – 40 Mhz and nanomolar concentration of the sample, the probability of registering more than one

photon in a single cycle is close to 0. A histogram with the number of photons collected as a function of time after the laser pulse shows photon emission distribution over the laser pulse cycle. From such distribution, it is possible to obtain the fluorescence lifetime of a probe, see Figure 2.3a. The fluorescence lifetime analysis allows to pre-filter the photon signal before FCS analysis.

Before each experimental session, the laser power was measured by a PM100 power meter (Thorlabs, USA) and set at a constant value for the whole measurement. Lab-Tek 8-Chambered cover-glass (Thermo Fisher Scientific, USA) was used as a sample container. Focal volume was set at a distance of 10 μm from the edge of the cover-glass. The temperature was maintained at constant temperatures ($\pm 0.5^\circ\text{C}$) within an isolating box enclosure with the temperature controller (OkoLab, Italy). Both FCS and TCSPC measurements were performed using the same confocal system.

The diode laser system with Pulsed Interleaved Excitation (PIE) mode was used to record a signal from ATTO488, and ATTO647N separately labeled strands. Blue and red laser pulses were produced every 50 ns. The blue pulse was delayed by 25 ns concerning the red one. The signal from labeled oligonucleotides was separated in terms of excitation time gates and fluorescence energy, see Figure 2.3b. The same optical pathway was used for both excitation and emission. The donor and acceptor signals were separated after reflection from the trichroic mirror (485 / 561 / 635 nm) by Chroma (USA) by a dichroic filter with a dividing edge of 640 nm. Finally, a band-pass filter (500 to 550 nm) was applied for the blue channel detector and a long-pass 645 nm filter for the red one. Custom-made Python scripts performed the analysis of raw photon counts for both channels [127–131]. The same setup was used for experiments performed on single labeled pairs.

Chapter 3

Results & Discussion

3.1 Equilibrium constant at subnanomolar concentration

In the case of physicochemical research, at nanomolar/picomolar concentrations, the complex formation process shifts towards the diffusion-limited case described by the Smoluchowski formalism and becomes analogous to the diffusional search problem [132, 133]. This represents a situation in which after the substrates find each other and react (to form a product), the number of these substrates is eliminated from the system. However, the formation of the non-covalent complex is a reversible process. After dissociation of a complex, two substrates may remain for some time in close proximity, compared to the average distance between them in the highly dilute solution. Therefore, an excursion effect may be expected, where multiple rebinding events can be observed [132, 134].

Therefore the initial part of this dissertation is addressed to the analysis of the biochemical complex formation, observation of possible anomalies (e.g., rebinding), and determination of its equilibrium constant at the subnanomolar concentration scale. As a model biochemical complex formation, the experiments proceeded on complementary oligonucleotide strands hybridization.

3.1.1 Selection of analysis method

In the initial phase of the project, purchased oligonucleotides were carefully studied by using FCS, see Figure 3.1. Hydrodynamic radii of oligonucleotides

in both single-strand and duplex forms were calculated based on obtained diffusion coefficients at 25°C, according to the Einstein-Smoluchowski equation.

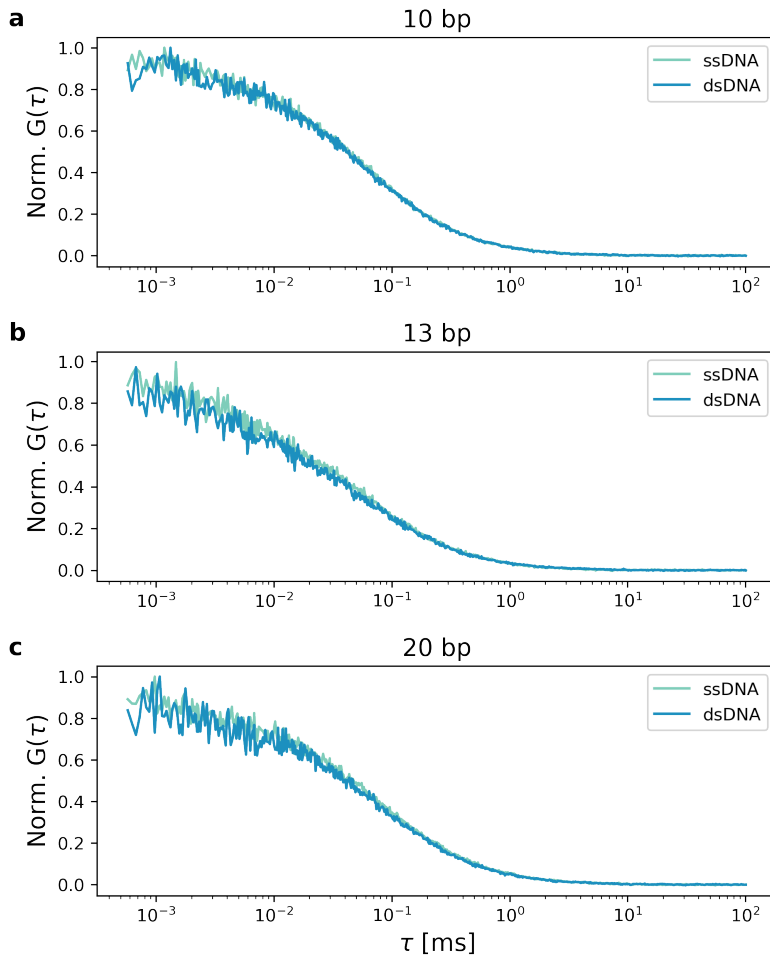


FIGURE 3.1: Autocorrelation curves recorded for purchased oligonucleotides in single and double stranded forms for **a** 10, **b** 13 and, **c** 20 bases in a sequence. According to obtained diffusion times diffusion coefficient of single strand were 174, 154 and 122 $\mu\text{m}^2/\text{s}$ for 10, 13, 20 bp oligonucleotides, whereas fully bounded duplexes diffusion coefficients changed to 173, 144 and 122 $\mu\text{m}^2/\text{s}$, respectively.

Hydrodynamic radii of labeled single strands of oligonucleotides were 1.4, 1.6, and 2.0 nm for 10, 13, and 20 base pairs, respectively. Upon complex formation (excess of the complementary strand), these values changed to 1.4, 1.7,

and 2.0 nm, respectively. Nevertheless, the differences in the radius between single and double stranded forms are of the order of 10%. Such moderate difference precludes quantitative estimation of the bound fraction based on FCS measurements. Therefore, instead of FCS, I focused on FRET as a primary technique throughout the initial research.

FRET experiments were based on the photon-intensity-based (ratiometric) FRET approach. After the donor excitation laser pulse, emission photons were recorded separately in the donor emission (500 – 550 nm) and acceptor emission (>645 nm) channels. By using custom-written Python scripts, raw data of photon counts were exported and as an average intensity (photon counts per second) for each channel [127–131]. These values were reduced by the background photon counts, recorded before each experimental session with the same buffer used in the experiments used instead of the sample. Considering this, the FRET efficiency was calculated as determined by Equation 1.14 (rewritten below). For this TCSPC system and selected labeled oligonucleotides, η was equal to 1.38.

$$F_{eff} = \frac{I_{acc}}{I_{acc} + \eta \cdot I_{don}} \quad (3.1)$$

Laser power was adjusted so that the photon count rate would never exceed 100 kilo counts per second (kcps) per channel. Typically, a single measurement lasted 30–60 seconds. In every control FRET experiment performed before each measurement at high ionic strength and DNA concentration, I observed absolute FRET efficiencies of at least 88% for all samples containing hybridized pairs. Even though the average distance between the dyes is much shorter than the Forster radius, 100% FRET efficiency was not reached. Based on recent studies, translational and rotational effects originated from the fact that the dyes are linked to DNA chains via around 1.5 nm long flexible tethers have been excluded as the reason for this effect [135, 136]. FRET efficiencies lower than 100% are most probably caused by the local quenching or other environmental effects. Measurements were performed at the same temperature as incubation, and great care was taken to keep the sample temperature constant at all times. For conditions where the reaction was relatively rapid

(equilibrium established within minutes), single-strand solutions were pre-heated before mixing them to the desired temperature. Data acquisition was then performed in a continuous mode, and only afterward was the raw signal split into 15 or 30 s bins. All samples for hybridization experiments were prepared with equal amounts of two complementary strands. For melting experiments, the starting point was a fully-bound duplex (100 µM solution of the hybridized double strand in TE buffer), which was diluted to the desired concentration in a buffer of choice. Bound fraction, θ (i.e., a fraction of the oligonucleotide population in the duplex state at a given moment) was calculated by dividing the measured FRET efficiency measured before the experimental run for the fully-bound duplex.

$$\theta = \frac{FRET_{(t)}}{FRET_{(\infty)}} \quad (3.2)$$

3.1.2 Single molecule experiments – surface adsorption

While performing the single-molecule measurements, it is necessary to control the concentrations of the substrates precisely. The experimental probe concentration may differ even by order of magnitude from the value calculated for a dilution series performed during the sample preparation, especially at nanomolar and subnanomolar concentrations of reactants. Such observations are typical for FCS measurements. The difference in concentrations is mainly caused by the adsorption of the probes on the phase border of the liquid sample (container walls and the solution/air interface).

This effect is pronounced for the hydrophobic part of the fluorescent probes. The example of oligonucleotides labeled with ATTO 647N dye also showed a high tendency towards accumulation at the phase border. In an experiment with 13 bp, ATTO 647N-labeled oligonucleotide diluted in PBS to a final concentration of 10 nM, the actual concentration measured by FCS was only 1.7 ± 0.3 nM. When focusing the confocal microscope on the cover glass surface, an increase of fluorescence intensity by up to two orders of magnitude versus the bulk intensity was observed, which suggested significant surface adsorption. To address this issue, one might decrease the surface adsorption of a fluorescent probe by two approaches:

- chemical modification/passivisation of cover glasses usually surfaces by PEG-coatings
- use of a surfactant (presenting no specific affinity to the fluorescent probe and reactants) at concentrations below CMC

A vivid example of both solutions was shown in the series of FCS experiments where ATTO 647N-labeled 13 bp oligonucleotide was diluted to the concentration of 10 nM. The oligonucleotide's bulk concentration in the PEG-coated sample measured by FCS was 3.1 ± 0.3 nM (i.e., still three times lower than the expected value). On the other hand, the addition of Tween 20 in the concentration of 0.002 weight% (corresponds to 16 μ M; CMC=60 μ M) showed no significant reduction in concentration (determined 11.4 ± 0.05 nM). The comparison of experimental series measured by FCS shows that each method (passivation or addition of surfactant) did not affect the equilibrium constant Figure 3.2a. The direct observation of oligonucleotide distribution within the sample after the addition of surfactant was observed by three-dimensional scanning. The 3D scans were performed over a cubic volume containing a part of the 10 μ L droplet with the 10 nM solution of the oligonucleotide. The Figure 3.2b indeed shows that the labeled DNA accumulated on the surface of the droplet.

The possible impact of the surfactant and its interactions with the probes cannot be neglected. Above the CMC, the hydrophobic parts of the probes may be incorporated into the micelles, which significantly complicates the equilibria observed between various entities in the sample [72]. I checked whether the surfactant's introduction might bias the results by introducing some stabilizing effect on the duplex. The control series of experiments were designed in such a manner: a fully diluted duplex of 13 bp strand of final concentrations equal to 0.1, 1, and 10 nM in pure 3 mM PB buffer was mixed with various amounts of Tween 20 (0.0002 -0.2 wt.%). The bound fraction was measured by using FRET after 24 hours of incubation at 25°C. The results are presented in Figure 3.2c. Neither the normally used 0.002% surfactant addition nor a 10 times greater amount of surfactant influenced the observed

bound fraction values. For 0.2% Tween 20, the duplexes were completely dissociate. There were no differences in the diffusion coefficients measured by FCS in the presence of 0.002% Tween20.

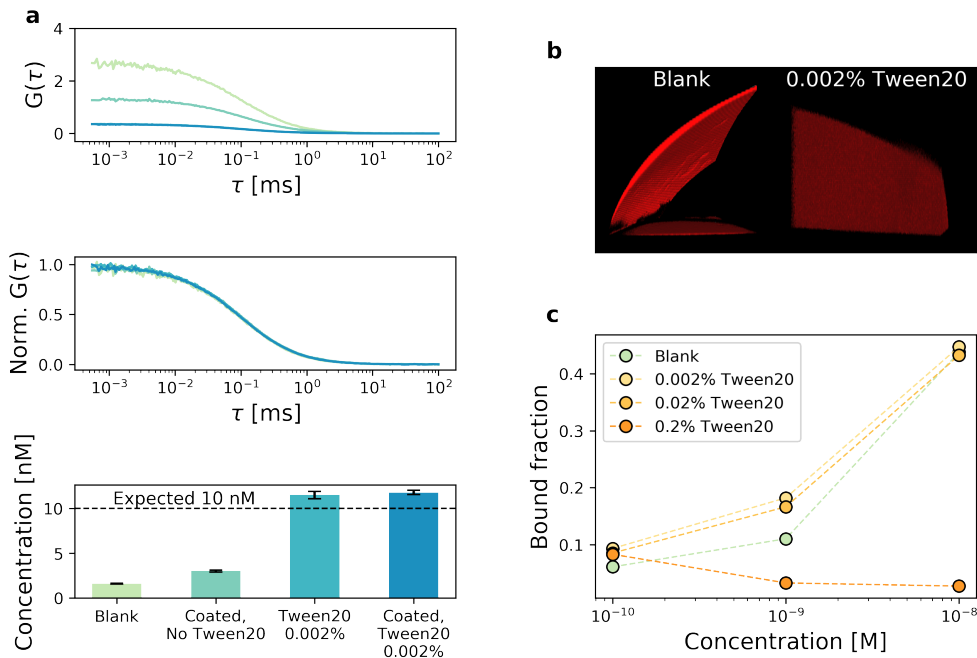


FIGURE 3.2: Comparison of PEG surface passivation and introduction of Tween20 as a method to prevent surface adsorption of the fluorescent probe. **a** FCS measurements shows the change of amplitude of autocorrelation function at $G(0)$ (the smaller amplitude, the bigger concentration) (upper panel). After normalization, no shifts towards short or long correlation times were observed for all measured samples (middle panel). The barplot presents the determined concentration in each setup and comparison with the expected value (bottom panel). **b** 3D scans of a cubic volume (edge length 1.3 mm) of fragments of droplets containing ATTO 647N-labeled 13 bp oligonucleotide at a concentration of 10 nM. In both cases, droplets were placed on an untreated coverglass surface. The oligonucleotide's significant adsorption is observed both on the coverglass and the air/sample interface in the absence of surfactant (left panel). Without surfactant, fluorescence intensity at the coverglass surface as well as sample/air interface is higher by at least an order of magnitude than the bulk intensity. Adsorption is suppressed by supplementing the sample with 0.002% Tween 20 (right panel). **c** Fraction of bound (duplexed) oligonucleotides after 24 hours of incubation in pure 3 mM PB buffer and same buffer supplemented with Tween 20 at concentrations of 0.002%, 0.02% and 0.2%.

The hydrophobicity of the dye is a key factor influencing its tendency to surface adsorption. During all of my research utilizing various dyes (families of Alexa Fluors, ATTOs, YOYOs, SYBR, anthracyclines etc.). To mitigate the probe adsorption on the sample/coverglass and sample/air interfaces, I would recommend applying suitable surfactant below CMC (presenting no specific affinity to the probes or any significant component of the system) instead of surface modification (as it is more laborious).

For all experiments included in this Ph.D. thesis, to control the concentration of labeled DNA strands, the addition of 0.002% of Tween 20 to the buffer was standard experimental protocol.

3.1.3 Apparent equilibrium constant

Kinetics of oligonucleotide melting and hybridization is rarely taken into account when optimizing protocols for biochemical procedures. However, at low oligonucleotide concentrations and ionic strengths, these processes may cause slow kinetics, which was previously predicted [137]. Ignoring this fact may be a source of significant errors in experimental results. I illustrated this on the example of measurement for the determination of the equilibrium constant.

The FRET was used to measure the bound fraction and the K constant for melting of the 13 bp duplex at 20°C, in a 10 mM PB buffer. Samples were prepared by diluting 10 μ M stock solution of a fully formed duplex and incubating them overnight. In an experiment performed on a broad range of final oligonucleotide dilutions (from 1 μ M down to 50 pM) the value of K should be independent of the samples' concentrations. With the K of the reaction of the order of 10^9 , the decrease in the bound fraction was observed with decreasing concentration. At subnanomolar concentrations – where the equilibrium should already be shifted towards the single strand form – the bound fraction flattened out at the value of around 0.6 As depicted in Figure 3.3, this leads to the observed K values being shifted by up to two orders of magnitude upwards from the expected value.

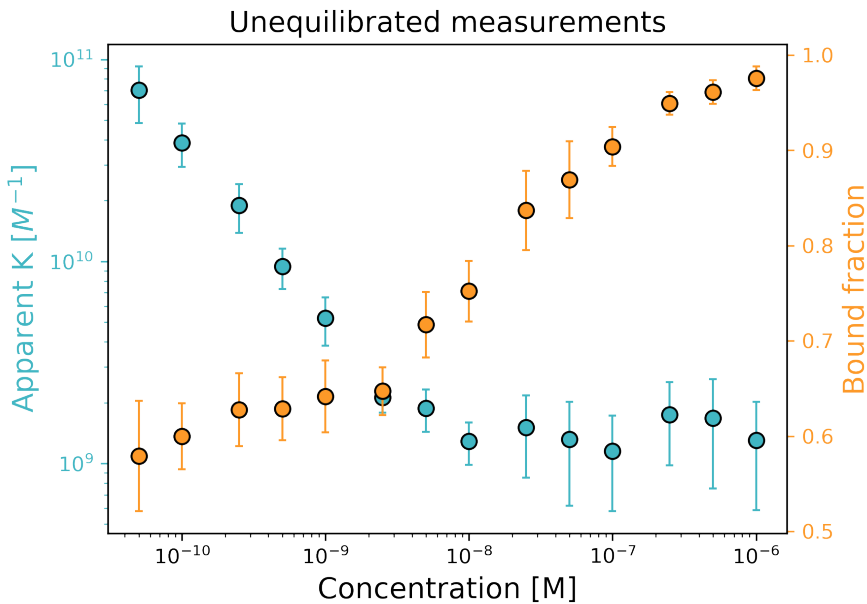


FIGURE 3.3: Bound fraction and apparent equilibrium constant calculated on its basis for 13 bp oligonucleotide melting. Samples were prepared by dilution of 10 mM stock solution of a fully bound duplex. For high concentrations, equilibrium establishes relatively quickly. The dilute solutions are not at equilibrium at the moment of measurement, yielding K values shifted by nearly two orders of magnitude from the expected value.

The results of the experiment shown in the Figure 3.3 seem to suggest that the equilibrium constant may depend on the concentration, especially in the high dilution limit. Complementary 13 bp strands at 1 nM are characterized by reaction radius $R_R = 3.2$ nm (which is sum of hydrodynamic radii of reaction components) and average distance between molecules L of around 583 nm, calculated as $L = \left(\frac{3}{4\pi N_A C}\right)^{\frac{1}{3}}$, where N_A is Avogadro number and the C is molar concentration of oligonucleotides [138]. In such a diluted system, the reaction radius is orders of magnitude smaller than the average distances between reagents. Therefore, there is a substantial time after dissociation of a pair of strands when the distance between them is much shorter than the mean distance between reagents observed in the solution. This may suggest that the unexpected dependence of K on the concentration is caused by re-binding phenomena (the same pair of substrate molecules may react multiple

times before the third molecule's arrival). Such a situation might be observed (on a small scale), for example, in multi-step protein modification, which might increase the equilibrium constant by decreasing the effective dissociation rate [134].

The role of rebindings was tested by performing computer simulations using enhanced Green's function reaction dynamics method (eGFRD) of a simple model reversible process $A + B \rightleftharpoons AB$ [139, 140]. The reaction parameters were set to values relevant to the oligonucleotide intrinsic rates of binding in the experiments, $k_a = 6 \times 10^7 \text{ M}^{-1}\text{s}^{-1}$ and $k_d = 0.1\text{s}^{-1}$. The in-depth details of the simulation are presented in the cited work [35]. The simulations confirmed that both effective association k_+ and effective dissociation k_- rates are renormalized by the rebindings, thus $k_+/k_- = k_a/k_d$ [141]. This result means that some molecules in the system may react multiple times, but in different parts of the reactor, molecules may, on average, wait much longer times for arrival than is expected. Therefore, statistically, such contradictory events are averaged, and equilibrium constants can not be dependent on concentration.

The simulation results contradict the hypothesis made based on the results presented in Figure 3.3. Thus, no deviations of the apparent equilibrium constant should be observed even at a highly high dilution of the reagents. The discrepancy observed in Figure 3.3 is instead originated from the fact that overnight incubation was not sufficient for the equilibrium to establish in all cases. An analogous experiment supported this hypothesis. The oligonucleotide bound fraction was observed for the 13 bp sequence over 19 days from the moment the initial(starting) dilution. As shown in Figure 3.4, the equilibrium for highly dilute solutions is reached only after several days of incubation at 20°C.

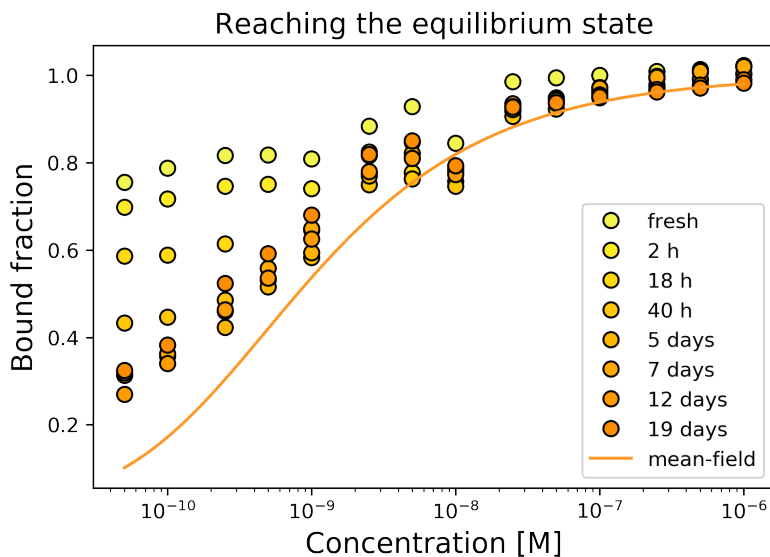


FIGURE 3.4: Bound fraction of a 13 bp oligonucleotide at 20°C in 10 mM PB buffer, observed for a range of concentrations over 19 days from the moment of diluting the 10 mM stock of fully-bound duplex to the target concentration. The orange line represents the predicted dependence of bound fraction on oligonucleotide concentration at equilibrium conditions. For concentrations below 500 pM, the equilibrium is reached by a period longer than a week.

The slow approach towards equilibrium was most pronounced in the low concentration range. However, the equilibrium solution composition was close to the starting point of fully bound duplexes for the high oligonucleotide concentrations. Therefore, to determine the equilibrium constant or the strength of the interactions, one must consider a substantial incubation time of reaction.

The approaching the equilibrium at the nano and subnanomolar concentration are long (several days) even for a reaction where K is in order of 10^9 M^{-1} .

3.1.4 Approaching the equilibrium from either substrates or product side

The establishing of the equilibrium can be analyzed by either forward or backward runs of the reaction. The reaction started either by diluting a concentrated (10 mM stock) solution of a fully-bound duplex or mixing two solutions of complementary strands. The changes were monitored in a function of a bound fraction over time. The strands of 10 bp were prepared at final concentrations of 10 nM and 100 nM in 3 mM and 10 mM PB buffer solutions. The results are presented in Figure 3.5. Irrespective of the reaction conditions, neither the final equilibrium state nor the process's dynamics depended on whether the reaction was started from substrates or product form. This served as another proof that the bound fraction obtained from the FRET experiments is indeed a manifestation of the reaction's inherent properties and not an artifact or error in the experiment design.

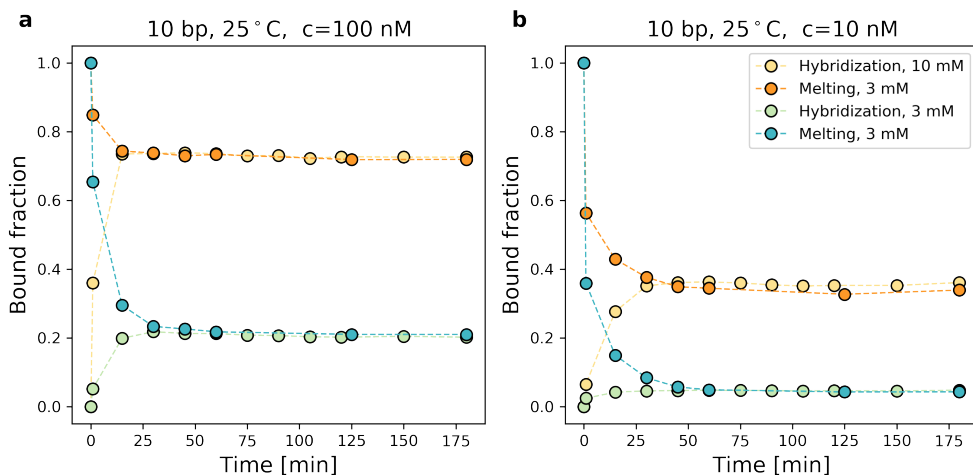


FIGURE 3.5: Bound oligonucleotide fraction over reaction time for systems starting from the single-strand-only state (hybridization) and double-strand-only (melting). 10 bp strands of the final concentration of **a** 100 nM and **b** 10 nM were incubated at 25°. At any given conditions, there was no difference in either the final composition of the system or the time necessary to reach the equilibrium between the forward and backward reactions. Legend applies to both panels.

3.1.5 Equilibrium constants, kinetics and activation energy

To determine kinetics and equilibrium constants, each sequence (10, 13, and 20 base pair) was examined in the reaction where equal volumes of two solutions of complementary strands of equal concentrations were mixed. The experiments were performed at 15, 25, and 35°C in two PB buffers concentrations 3 mM and 10 mM. To cover the whole range of K (for border conditions $\Delta K = 10^5$) at each set of conditions, the strands' concentrations were tuned for each set of conditions. In this way, the equilibrium could be shifted towards either the single or double strands and keep the bound fraction in a range between 0.1 and 0.9 throughout the measurements. The experimental errors in the measured FRET efficiency could cause substantial shifts in the K determination outside this range. To keep the bound fraction in the experimental regime (between 0.1 and 0.9), for given strand pair (10, 13, or 20 bp) and experiment conditions (temperature and ionic strength) initial concentrations of DNA was preliminary tested depending on bound fraction value at equilibrium ($t \rightarrow \infty$). All reactions were conducted for a period of time well beyond the time necessary for the equilibrium to establish. The results of the experiments are summarized in Figure 3.6.

The K increases with the sequence length and ionic strength and decreases with temperature. The temperature dependence is most pronounced for the shortest sequence of 10 bases (~100 times decrease of K by 20°C difference). This seems to be in line with the predictions of the basic model of oligonucleotide melting [99]. Quantitative application of the model for prediction of melting temperature, T_m is not feasible. The values of T_m predicted for the 10, 13, and 20 bp strands were 30, 38, and 52°C, respectively. The temperature range that I applied in the experiments was 15 – 35°C. For most of the samples, equilibrium was shifted towards either high or low bound fraction at any of the studied temperature, simply by manipulating the strand concentration and solution ionic strength. The T_m is defined as a temperature at which the equilibrium bound fraction is 0.5. Therefore, it is impossible to give a single T_m value for any given sequence without specifying the conditions.

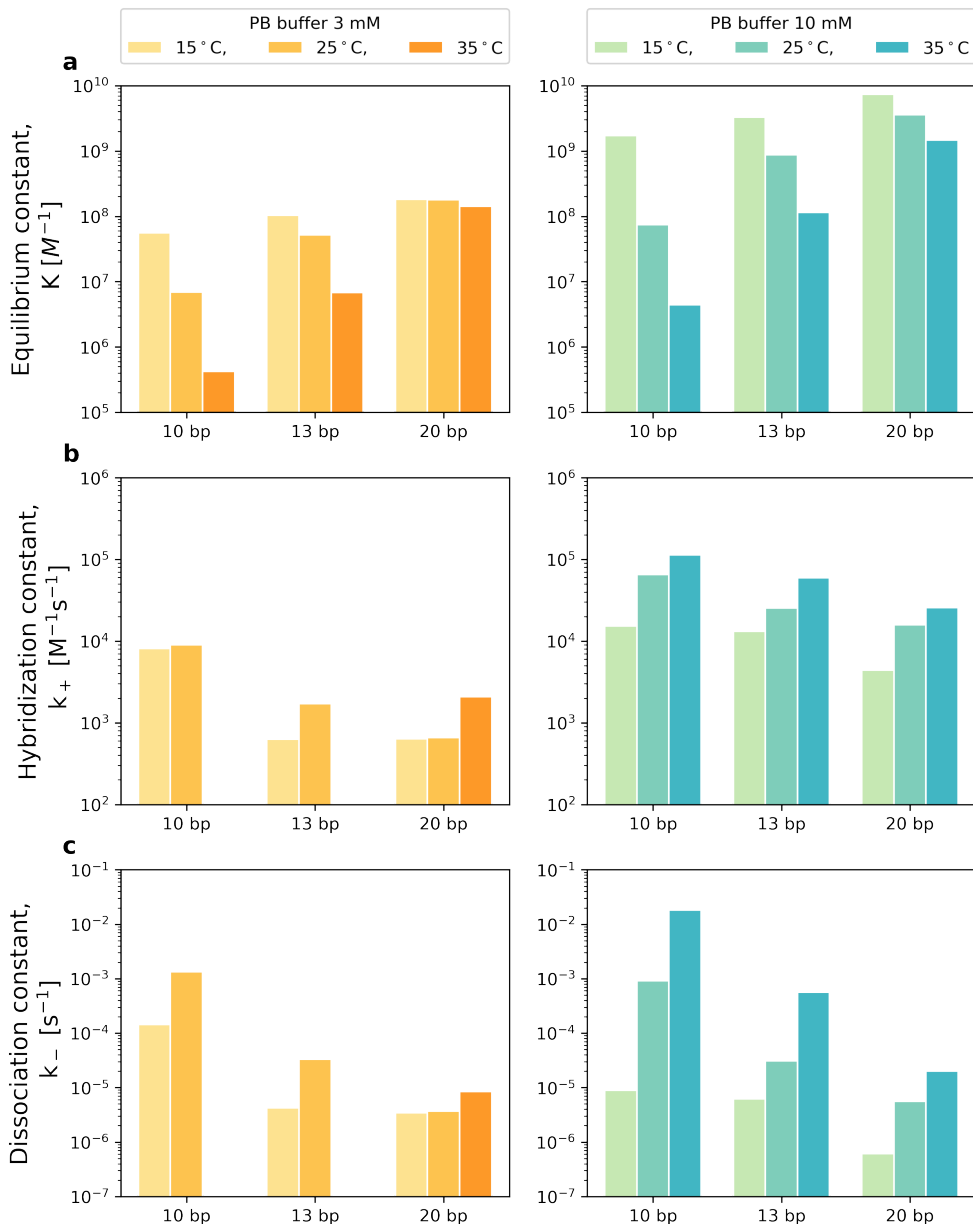


FIGURE 3.6: Summarized results over series of experiments. **a** Equilibrium constants K , **b** hybridization rate constants k_+ and, **c** melting rate constants k_- for the three studied sequences of length of 10, 13, and 20 bases. Left hand side concerns reactions in 3 mM PB buffer, right hand side – 10 mM PB buffer. All results are based on FRET measurements. Kinetic constants are missing for 10- and 13-base sequences in 3 mM buffer at 35°C. It was caused due to very low binding between the strands and, in consequence, difficulties in reliable quantitative analysis of the results.

At all studied conditions, the hybridization rate increased with temperature. This indicates positive activation energy for the reaction. Some previous studies showed that hybridization might be a negative activation energy process [107, 110, 142]. The negative activation energy was mostly observed at temperatures around T_m , where nucleation is considered the rate-limiting step. Therefore after dissociation, the increase of the temperature prevents successful bonding of the initial contacts, hence duplex formation does not proceed. At low temperatures, the limiting step was considered diffusion-controlled, and thus the sign of E_a changed to positive. This held across the whole studied concentration range, from picomolar to sub-millimolar oligonucleotide solutions. Moreover, k_+ increased by around an order of magnitude when moving from 3 mM to 10 mM buffer. Based on those results, the critical factor here is the electrostatic interactions between the oligonucleotide backbones. This phenomenon of regulation of the hybridization rate was suggested before [137]. The dependence of strand dissociation rate on temperature is much stronger than for hybridization rate, which results in an overall decrease of equilibrium bound fraction with temperature for any given system. The results indicate that duplex formation is in line with a simple Arrhenius model with positive activation energy.

3.2 Brightness analysis method

During the experiments with long incubation periods, the pulsed interleaved excitation scheme enabled us to monitor the acceptor labeled strand's concentration independently and whether it remains constant over time. The laser excitation scheme allows to separate time gates of excitation pulses (485 nm and 635 nm; blue and red) and detector channels. In total, data could be separated by four possible combinations (two time gates and two colors), see Figure 2.3b. Data from each time gate were then analyzed separately. Interestingly, the acceptor's brightness labeled changed significantly (even by a factor of two and a half) upon binding to the complementary strand, see Figure 3.7. In an ideal system where FRET efficiency is 100%, no corrections are needed (parameter $\eta = 1$), no leakage and, no photon surplus is observed; this value should be two. Classical FRET theory does not predict such observations.

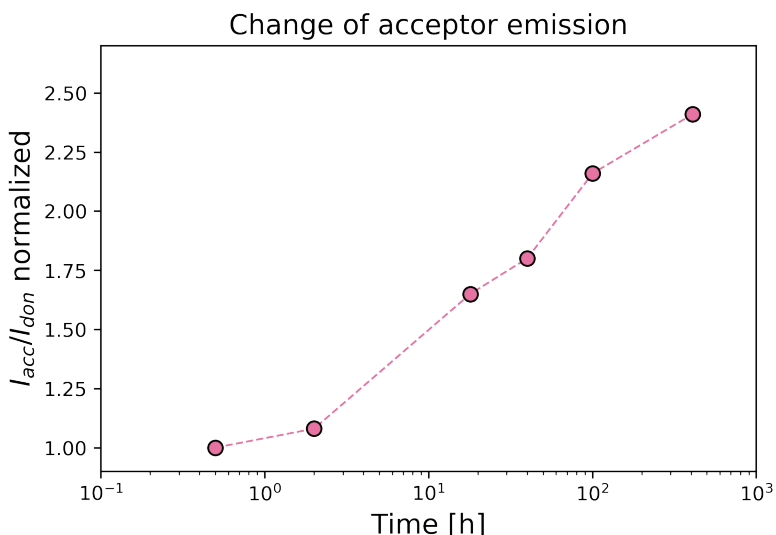


FIGURE 3.7: Changes in the number of photons per second were recorded for the acceptor emission channel after its direct excitation for the duplex melting reaction. Photon count rates are normalized to the value recorded at the first time point. This exemplary data concerns the melting of a 13 base pair duplex diluted to 0.1 nM in 10 mM PB buffer and incubated at 25°C.

During FRET analysis, after complex formation, the local environment

around the fluorophores (donor and acceptor) changes. Influence of environment may change the molecular brightness (MB) of dyes. The difference is corrected by performing two experiments separately, where donor and acceptor labeled substrate is mixed with a corresponding non-labeled substrate.

Therefore in brightness analysis, results were independently analyzed by the notion of MB, defined as the number of photons emitted per second per fluorophore molecule under given experimental conditions. The magnitude of MB changes may be vast if the changes are dramatic (e.g., change of solvent, covalent bonding to some other molecule) or if new relaxation pathways are opened (e.g., fluorescence quenching, resonance energy transfer). Those changes have already been used for viscosity sensors development, and ion concentration indicators [143–145]. However, even moderate modulation of the fluorophore’s surroundings – such as complex formation – may affect MB to a measurable extent. This observation created foundations for a new analytical method, with possible applications in photon-counting-based biochemical techniques.

The method pursues an alternative approach to FRET for determining the strength of interactions of the formation of non-covalent complexes. This method’s basis is MB, which is determined by measuring the total number of photons N_p emitted from the known volume V_0 (e.g., the focal volume of a confocal microscope) at the given fluorophore concentration (e.g., determined by FCS). The MB is calculated via a simple relation $\frac{N_p}{V_0 \cdot C} = \text{MB}$.

The complex-forming reaction presented on an example of hybridization reaction of a complementary DNA strand can be written as $A+B \rightleftharpoons AB$, where (A) is labeled oligonucleotide strand and (B) is non-fluorescent complementary strand. In the solution of only labeled strands, the total number of emitted photons is proportional to the time of signal acquisition t and the concentration C_A of the labeled strand of an intrinsic molecular brightness α , excited inside the focal volume V_0 . The average number of photons emitted per unit time defines the count rate, χ_0 :

$$V_0 \cdot \alpha \cdot C_A = \frac{N_{\text{photons}}}{t} = \chi_0 \quad (3.3)$$

After addition B the complex AB is formed. Now in the reaction pool the

only fluorescent components in a solution are A and AB . Therefore Equation (3.3) takes the form:

$$V_0 \cdot (\alpha \cdot C_A^{eq} + \gamma \cdot C_{AB}^{eq}) = \chi_1 \quad (3.4)$$

When complex AB is formed, the intrinsic brightness of fluorophore, α changes to γ . In Equation (3.4) C_A^{eq} and C_{AB}^{eq} are equilibrium concentrations of reagents in the mixture, related by the equation $K = \frac{C_{AB}^{eq}}{C_A^{eq}C_B^{eq}}$. Because $C_A = C_A^{eq} + C_{AB}^{eq}$ and $C_B = C_B^{eq} + C_{AB}^{eq}$ we get the relation:

$$K = \frac{C_{AB}^{eq}}{(C_A - C_{AB}^{eq}) \cdot (C_B - C_{AB}^{eq})} \quad (3.5)$$

Equation (3.5) is analytically solved to determine the equilibrium concentration of complex C_{AB}^{eq} . C_{AB}^{eq} is the function of three experimentally known variables,

$$\begin{aligned} C_{AB}^{eq} &= f(C_A, C_B, K) = \\ &\frac{1}{2} \cdot (C_A + C_B + \frac{1}{K} - \sqrt{(-C_A - C_B - \frac{1}{K})^2 - 4 \cdot C_A \cdot C_B}). \end{aligned}$$

Finally, the Equation (3.4) is rewritten as:

$$V_0 \cdot \alpha \left[C_A - C_{AB}^{eq} \right] \left[1 + \frac{\gamma}{\alpha} \cdot K \cdot \left(C_B - C_{AB}^{eq} \right) \right] = \chi_1 \quad (3.6)$$

Equation (3.6) relies on parameters that can be obtained experimentally:

- confocal volume V_0 is defined during system calibration under given experimental conditions,
- both α and the initial concentration C_A of the fluorescent substrate are determined in a single FCS measurement according to Equation (3.3),
- brightness γ is determined in an experiment in which substrate B is in high excess to the concentration of A .

As the $\frac{C_B}{C_A}$ ratio increases, the $\chi(C_B)$ function begins to take the shape of the Langmuir isotherm (for $\alpha < \gamma$) or its inverse ($\alpha > \gamma$), see Figure 3.8.

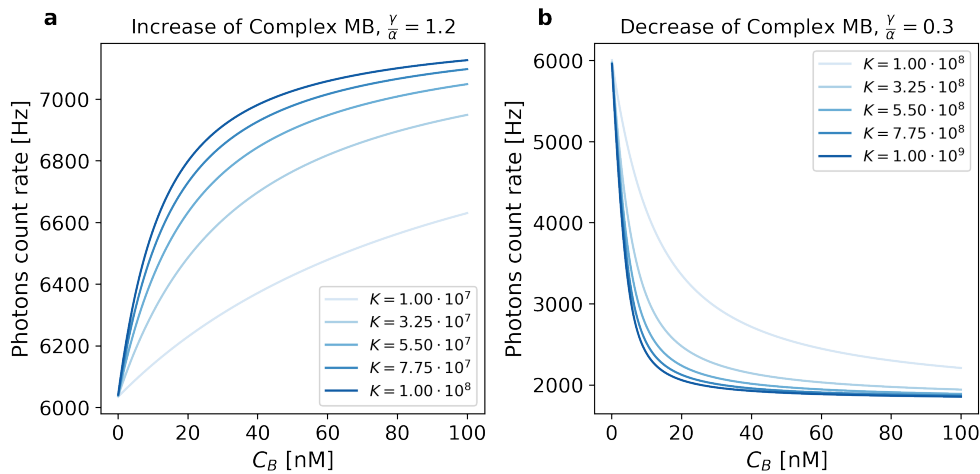


FIGURE 3.8: An example of the function described by the Equation 3.6 for the reaction where the molecular brightness of the complex **a** increases or **b** decreases relatively to the labeled substrate.

FRET — became a general technique in biochemical measurements as it combines substrate sensitivity at picomolar concentrations, nanoliter sample volume, and short time of data acquisition (in order of seconds). However, FRET requires to label two substrates with two different dyes (donor and acceptor of energy). Additionally, two dyes need to be in close proximity within the complex (<10 nm).

Brightness analysis simplifies the FRET method to operate by **using only one intrinsically fluorescent (or labeled) substrate** without losing its generality. This method leverages the fact that a dye's brightness is a parameter that changes upon contact with other probes [145, 146].

3.2.1 Validation by FRET

The use of FRET for biological research has become a standard in laboratories. Thus, to validate the brightness method, FRET was used as a benchmark. Here, the intensity approach (based on the number of photons transferred

from the donor channel to the acceptor one) was used. One might apply a fluorescence lifetime approach to measure FRET efficiency via the FRET-induced decrease of donor fluorescence lifetime. However, in the case of determining K through analysing samples at different ratios of substrates, fluorescence lifetime histogram is composed of two overlapping populations fluorescence lifetimes. This implicates troublesome experiment design and further data analysis for proper separation of residual molecules of donor-substrate and formed complex lifetimes.

To calculate binding isotherm for reaction $A + B \rightleftharpoons AB$, the concentration C_{AB}^{eq} of complexes at equilibrium from FRET efficiency has to be estimated from the relation:

$$\frac{F_{eff}}{FRET_{MAX}} = \frac{C_{AB}^{eq}}{C_{AB}^{MAX}} \quad (3.7)$$

where, $FRET_{MAX}$ is maximum absolute FRET efficiency measured in the same experimental conditions, where acceptor molecules are in the significant excess over the donor ($C_B \gg C_A$). Therefore C_{AB}^{MAX} is the initial concentration of the donor labeled strand C_A . Measurements carried out in such conditions result in obtaining binding isotherm described by:

$$F_{eff} = \frac{C_{AB}^{eq} \cdot FRET_{MAX}}{C_A} \quad (3.8)$$

The equilibrium constant K could be determined by FRET using two pairs of double-labeled oligonucleotides. Designed pairs have donor and acceptor dyes either on the same end (3'488/647N) of the formed complex or on the opposite sides (488/647N), see Figure 3.9. Due to labeling dyes' different spatial distribution, the oligonucleotides pairs possess different FRET efficiencies (longer distance between fluorophores). The $FRET_{MAX}$ was determined, as 0.88 and 0.34 for 3'488/647N and 488/647N pairs, respectively. The sets of measurements were performed at different initial concentrations of the donor strand C_A for both pairs from 10 pM to 30 nM. After fixing the concentration of the donor-labeled strand, the concentration of the acceptor-labeled strand was varied.

Both FRET and brightness analysis methods were performed at different ratios C_B/C_A . Each point in the series has to reach equilibrium. The time of incubation of the sample should be considered for the lowest concentration of substrate.

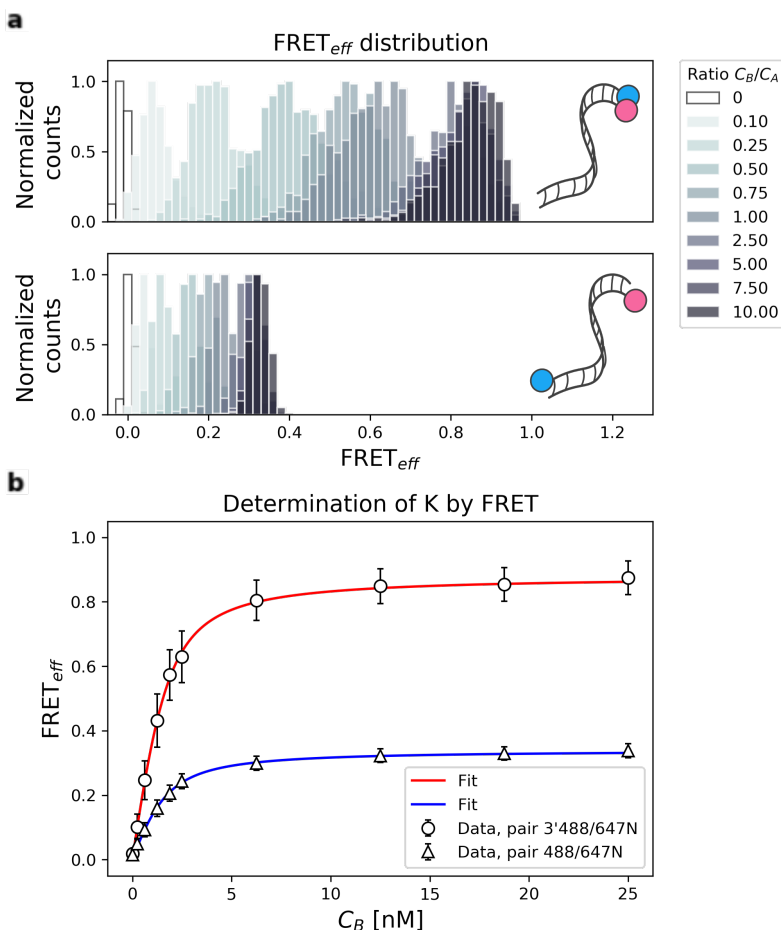


FIGURE 3.9: An example of FRET efficiency analysis of the sample where concentration of donor strand $C_A = 2$ nM: **a** histograms for series of samples in different ratio C_B/C_A binned with 100 ms interval for double labeled oligonucleotide pairs on the same sides (3'488/647N, top panel) and on the opposite sides (488/647N. bottom panel), **b** the determination of equilibrium constant for a given pair by fitting Equation (3.8).

During the fitting, two parameters have released the concentration C_A and

equilibrium constant K . The average equilibrium constant was determined for the broad range of concentrations. K were equal to $(3.5 \pm 1.9) \cdot 10^9 \text{ M}^{-1}$ and $(1.1 \pm 0.5) \cdot 10^9 \text{ M}^{-1}$ for 3'488/647N and 488/647N pairs at 25°C, 20 mM PB (pH=7.4) buffer, respectively. This value is in good agreement with our previous results in 10mM PB buffer at the same temperature [35]. The difference in values suggests that the same-end labeled pair has extraordinary attraction. This dye-dye interactions additionally stabilize the complex, which probably originates from Van der Waals interactions between polyaromatic dyes.

3.2.2 Molecular brightness analysis of single labeled pairs

The pairs where only one complementary strand is labeled can no longer transfer the energy as stated in the FRET theorem. The pairs named 3'488/NN and NN/647N (see Figure 2.1) were excited by using a wavelength of 485 (blue) and 635 (red) nm pulsed laser, respectively. In calibration experiments, V_0 for blue and red lasers were 0.280 and 0.440 fL, respectively. From the FCS measurements, the molecular brightness α was determined for each labeled strand without a complementary strand. These values were 13000 and 3600 counts per second per molecule for strands labeled with ATTO488 and ATTO647N, respectively. The brightness of the complexes, γ , was determined with a significant excess of complementary oligonucleotide strands. The molecular brightness increased by 22% for the 3'488/NN pair complex, while for NN/647N, it decreased 5%. The equilibrium constants for each pair were carried out in series of titration experiments where a constant concentration of labeled strands in the range of 10 pM to 30 nM was varied by non-labeled strand. In Figure 3.10, as the concentration of complementary strands in the mixture increases, the number of complexes formed increases, which can be seen from the change in the total number of photons counted by the detector. In the 3'488/NN pair, it was possible to determine equilibrium constants even at a concentration of 80 pM of colored strand, see Figure 3.10b. Due to such spectral behavior of ATTO647N and limited detectors sensitivity, the equilibrium constant could only be estimated for concentrations of labeled strand bigger than 10 nM. During the fitting, the calculated average equilibrium constants for both pairs were equal to

$(1.11 \pm 0.9) \cdot 10^9$ and $(0.9 \pm 0.4) \cdot 10^9 \text{ M}^{-1}$, for 3'488/NN and NN/647N pairs, respectively.

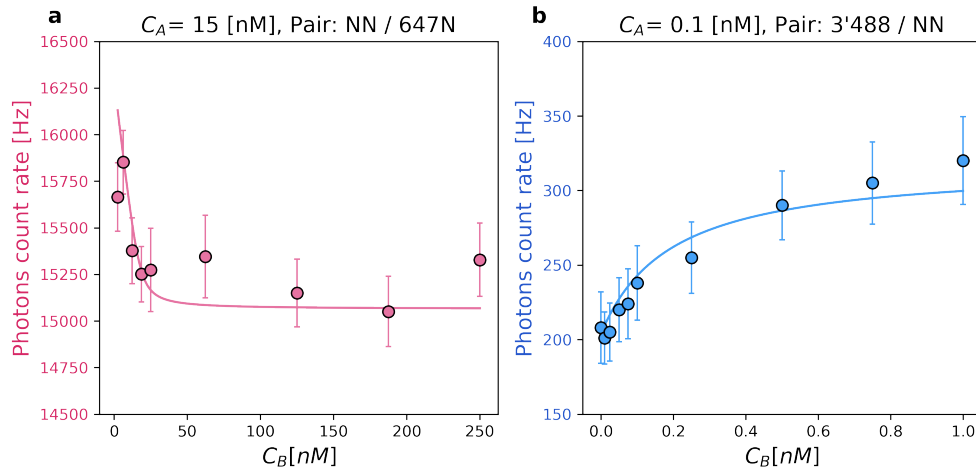


FIGURE 3.10: Exemplary results of the brightness change analysis for single-labeled oligonucleotide pairs. **a** For ATT0647N complex a 5% decrease in brightness of the complex is observed. **b** The complex formed by the reaction of the ATT0488 labeled strand with the unlabeled complementary pair increases the molecular brightness by 22% relative to the initiating strand of the substrate.

3.2.2.1 Experiments performed on double-labeled oligonucleotide pairs

The brightness analysis method was used to analyze the same data obtained during FRET validation. Photons were recorded upon blue excitation pulse for both red and blue channels. Thus, from the FCS analysis, it was possible to determine the brightness of each component of the reaction. In brightness analysis, an increasing intensity was observed in the red channel, whereas in the blue one, it decreased. This trend was in good agreement with the energy transfer mechanism. Such schematical approach is presented in Figure 3.11.

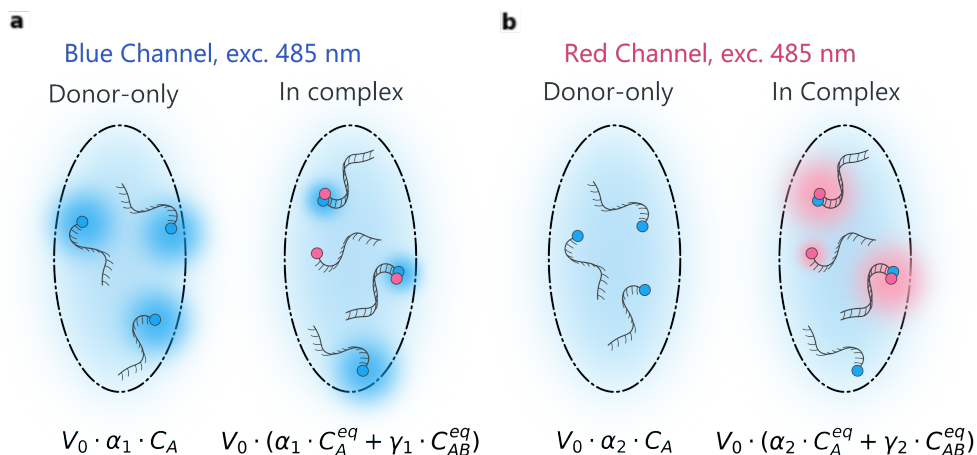


FIGURE 3.11: Labeled oligonucleotides before and after hybridization, excited in blue laser focal volume. Each situation can be analyzed either by blue or red channel. The fluorescence photons emitted by the complex can be visible in blue and red channels. **a** In the blue channel, the sample with the only donor has the background-corrected count rate proportional to brightness and initial concentration of oligonucleotides. After the addition of the acceptor-labeled strand, the sample begins to reach equilibrium. The formed complex possesses decreased brightness due to energy transfer between strands. Therefore overall count rate is decreasing. **b** In the red channel analysis, due to the spectral properties of donor-strand, brightness is close to the background signal. After hybridization, transferred energy can be emitted as photons by the acceptor molecule, and hence complex brightness is increased. The scheme is not drawn in scale.

The equilibrium constant K values for both red and blue channels recorded data were obtained by fitting the Equation (3.6). The data was obtained for the same broad range of concentrations as in FRET validation. The analysis was successful even at a concentration of around 100 pM, Figure 3.12a. The average equilibrium constants from all experimental series for 3'488/647N and 488/647N labeling pairs are $(3.4 \pm 1.1) \cdot 10^9$ and $(1.2 \pm 0.8) \cdot 10^9 \text{ M}^{-1}$, which are in good agreement with FRET ($3.5 \cdot 10^9$ and $1.1 \cdot 10^9$, respectively). The comparison of K values determined by either FRET or brightness analysis method for double-labeled pairs are shown in Table 3.1.

TABLE 3.1: Equilibrium constants K determined using the FRET and brightness method for double-labeled DNA strands.

	$K \cdot 10^9 \text{ M}^{-1}$	Brightness Method	
	FRET	Blue Channel	Red Channel
3'488/647N	3.5 ± 1.9	2.9 ± 0.9	3.9 ± 1.1
488/647N	1.1 ± 0.5	0.9 ± 0.7	1.4 ± 0.9

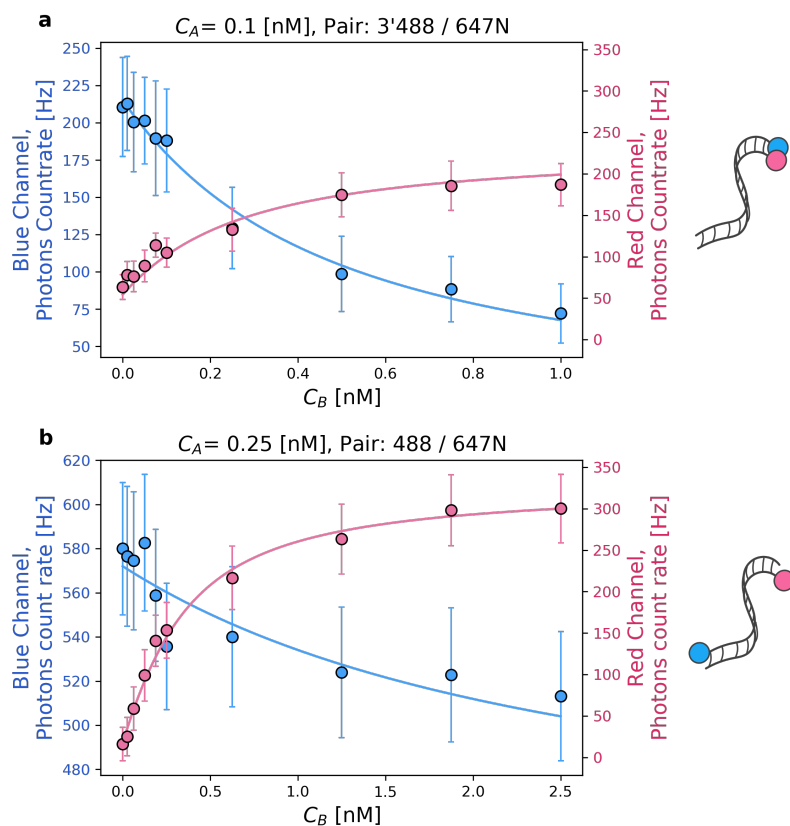


FIGURE 3.12: Double labeled oligonucleotide pairs analyzed by changes of molecular brightness for **a** 3'488/647N and **b** 488/647N. The molecular brightness is measured as a function of count rate. It is observed either by an increase in the recorded number of photons in the red channel or a decrease in the blue one.

3.2.3 Brightness analysis - Experimental errors

The established brightness method can be affected by different experimental errors (especially during sample preparation). The most common is not properly determined concentrations of either labeled or non-labeled substrate (especially $\frac{C_B}{C_A}$ ratio) or recorded intensity, χ . To estimate how such errors affect the determination of K different approaches may be considered. The first take advantage of the total differential approximation to estimate the total/maximum experimental error, $\sigma(K)$. Therefore the Equation 3.6 should be transformed from $\chi(C_A, C_B, K)$ to $K(C_A, C_B, \chi)$, see Equation 3.9.

$$\sigma(K) = \left| \frac{\partial K}{\partial C_A} \right| \cdot |\sigma(C_A)| + \left| \frac{\partial K}{\partial C_B} \right| \cdot |\sigma(C_B)| + \left| \frac{\partial K}{\partial \chi} \right| \cdot |\sigma(\chi)| \quad (3.9)$$

However, the Equation 3.9 contains the implicit function, $f(C_A, C_B, K)$ which makes impossible to analytically solve $\sigma(K)$.

The second estimation of $\sigma(K)$ is based on the Monte Carlo simulations, where multiple data can be generated, fitted, and then statistically analyzed. The self-written program utilizes one of the previously measured and fitted data series for pair 3'488/NN [127–131]. The molecular brightness α and γ were estimated in separate sets of measurements with an error of around 1%. Therefore it is treated as a constant value. The molecular brightness ratio was set to $\frac{\gamma}{\alpha}=1.23$. Through the analysis of a data series for a given C_A concentration, the average errors for substrate concentration $\sigma(C_B)$ and count rate $\sigma(\chi)$ were estimated as 15% and 5% respectively.

In order to determine the error of $\sigma(K)$, the error values from the normal distribution of $\sigma(C_B)$ and $\sigma(\chi)$ were drawn. They were applied for the entire data series, see Figure 3.13 separately to each point in the series. The Equation 3.6 was fitted ten thousand times ($N=10000$) for each generated series. All of the obtained C_A and K fitted values were averaged with calculated error through standard deviation.

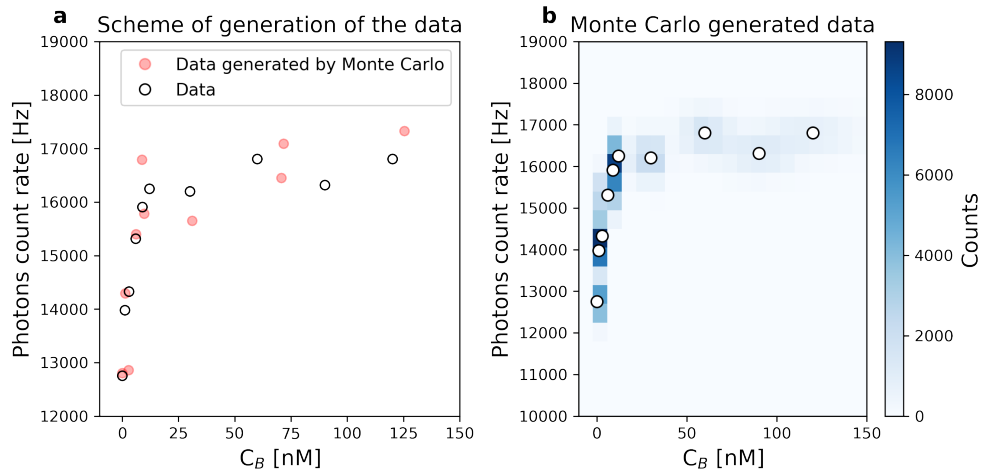


FIGURE 3.13: The $\sigma(K)$ estimation based on randomly generated experimental errors by Monte Carlo simulations. **a** Example of single generated data. **b** 2D histogram of ten thousand generated data series.

The fitting values for non-modified data series were $C_A=6.31 \pm 0.01$ nM and $K=(1.06 \pm 0.71) \cdot 10^9$ M⁻¹. Through the simulations obtained K value was equal to $(1.15 \pm 0.67) \cdot 10^9$, see Figure 3.13b. These results are in good agreement with the averaged errors obtained experimentally $(1.11 \pm 0.9) \cdot 10^9$.

The $\sigma(\chi)$ is related to the instrumental characteristics of the detector, i.e., noise level, dead time, sensitivity at a given wavelength of collected photon, and proper filtration of the background. The lower the concentration the higher is $\sigma(\chi)$. By increasing the number of data points for given ratio $\frac{C_B}{C_A}$ the impact of experimental and instrumental error can be reduced.

The critical attention should be paid towards correct preparation of initial substrates solutions (C_A and C_B).

3.2.4 Sensitivity of molecular brightness analysis for single and double labeled pairs

The analysis of molecular brightness of a fluorophore is sensitive to changes in the local environment around it. The observed difference of the MB of both ATTO dyes in both single labeled strands upon complex formation can be attributed to the known effect of DNA-DNA non-covalent π - π stacking [147]. Upon hybridization, parallelly arranged base pairs interfere with the HOMO-LUMO gap of dyes by changing local electron density, which causes either lowering or increasing the gap distance. The common sensitive part responsible for MB changes upon fluctuation of local environment are delocalized electrons in chromophore aromatic structure. Such effects are observed in many examples of commercially available dyes, i.e., SYBR, DAPI, YOYO, or even anticancer drug doxorubicin [9, 148, 149]. The change of molecular brightness may be observed in Figure 3.14, where emissions spectra of labeled oligonucleotides are recorded by spectrophotometer. The single-strand sample was 50 nM, whereas the double-strand was a mix of the initial strand with 10 times excess of a complementary strand. There was not observed the change in shape or shift of the maximum emission peak.

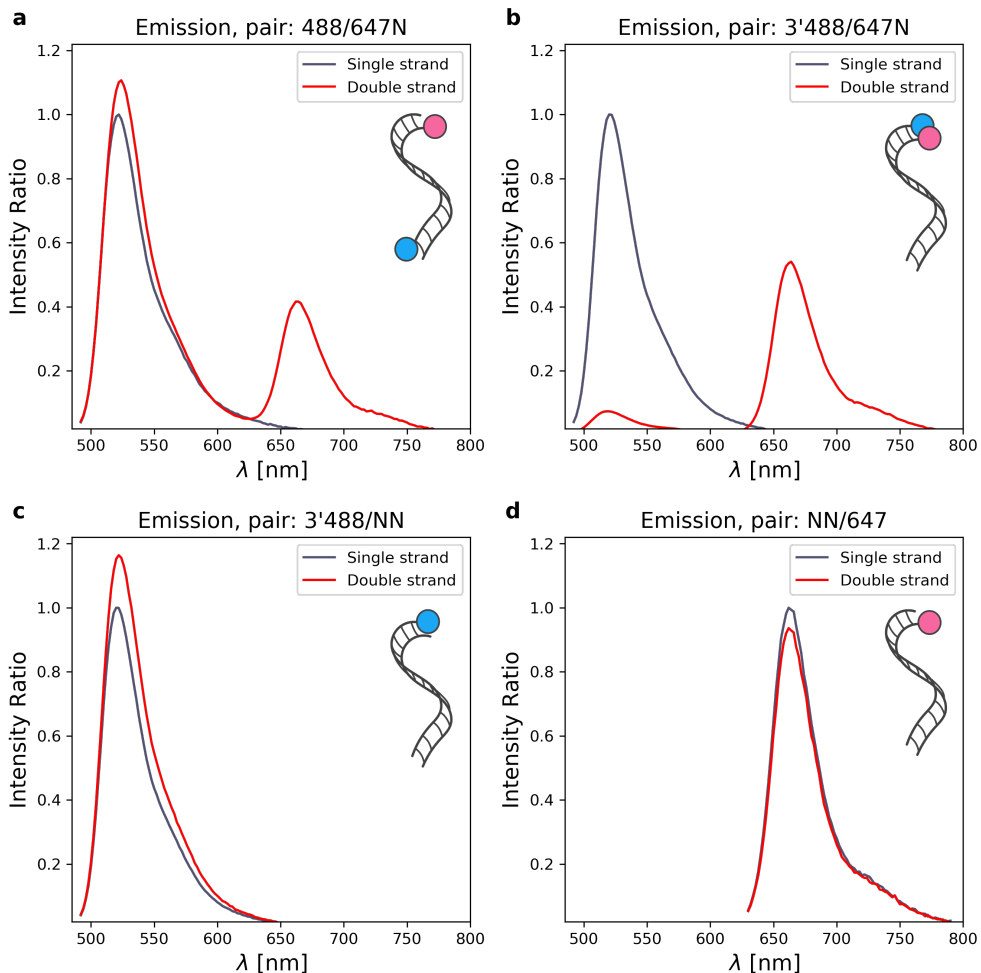


FIGURE 3.14: Emission intensity ratio of single strand to duplex form for double labeled pairs **a, b** and for single labeled pairs **c,d**.

Additionally, the FCS analysis in parallel to the intensity analysis for acceptor direct excitation was performed. It showed no change in total bulk concentration of the acceptor-labeled strand over time (information on concentration is retrieved from the amplitude of the autocorrelation function, which in principle does not depend on the probe's changes brightness nor size (for both single and double-strand forms). The influence of molecular brightness in any fluorescence studies is crucial to the obtained results to be taken into account indirectly as a correction factor and cannot be neglected.

The FCS measurements are usually used to determine either concentration or diffusion coefficients and the possible number of fluorescent components in the system. Figure 3.1 shows that it is not possible to separate fractions between single and double-stranded forms using diffusion coefficients.

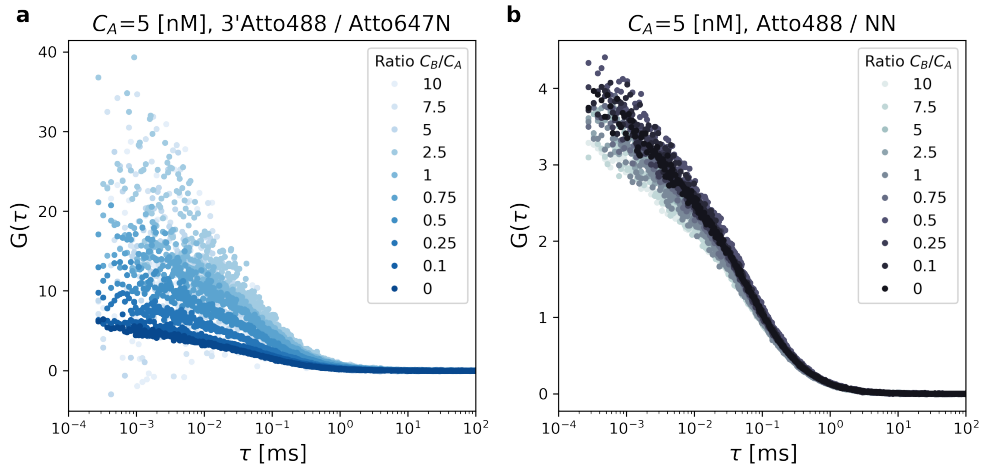


FIGURE 3.15: Series of FCS measurements for oligonucleotide pairs excited by the blue laser (485 nm) and recorded in the blue channel for **a** FRET pair ATTO488 labeled strand with ATTO647N complementary strand, and **b** ATTO488 labeled strand with nonlabeled complementary strand.

In the experiments at different $\frac{C_B}{C_A}$ molecular brightness, FCS may also falsify obtained concentration without proper understanding of the system's interactions. This can be presented on typical data series obtained during brightness or FRET analysis although analyzed by FCS, see Figure 3.15. In the case of double-labeled pair (3'488/647N, $K=3.3 \cdot 10^{-9} \text{ M}^{-1}$), the concentration of the donor should decrease 65 times between the ratio $\frac{C_A}{C_B}=0$ and $\frac{C_A}{C_B}=5$, but from FCS analysis it decreased only 5 times. Similar inconsistency in concentration may be observed for single labeled pair (488/NN), see Figure 3.15b. Also, in 488/NN, the molecular brightness is increased by $\sim 20\%$, while for 3'488/647N, the decrease was observed. This also affects the analysis of ACF as an artefact showing the increase in concentration.

Using FCS, it is impossible to separate a fluorescent substrate's fractions and form complex with a similar diffusion coefficient but with different molecular brightness (inseparable time-correlated components). In the complex formation of same length oligonucleotides, the FCS analysis allows only to precisely determine molecular brightness (expressed in a number of emitted photon per molecule per acquisition time) for:

- solely fluorescent substrate A,
- complex AB in the experiment when substrate B is in huge excess.

Molecular brightness may enable to provide insight of reaction mechanism [8]. **The molecular brightness is sensitive for any fluctuations in a local environment. Thus, all secondary interactions for a given system should be predefined and known before analysis.**

The comparison of differences in K values among all four oligonucleotide pairs (two double and two single labeled) shows an additional attraction between dyes themselves in the case of the 3'488/647N pair. The pair 3'488/647N showed three times higher K than other pairs. The comparison of equilibrium constants obtained for four differently labeled pairs of oligonucleotides was shown in Figure 3.16. This effect is most probably related to the $\pi-\pi$ stacking of ATTO dyes aromatic groups located at the same end of the formed complex. The binding energy calculated as the difference in Gibbs free energy is about $\Delta G = -2.75 \text{ kJ}\cdot\text{mol}^{-1}$. This value is bigger than energy of thermal fluctuations in the system $k_B T = 2.48 \text{ kJ}\cdot\text{mol}^{-1}$ at 25°C . Obtained ΔG value is in good agreement with stacking energy between polyaromatic groups [150].

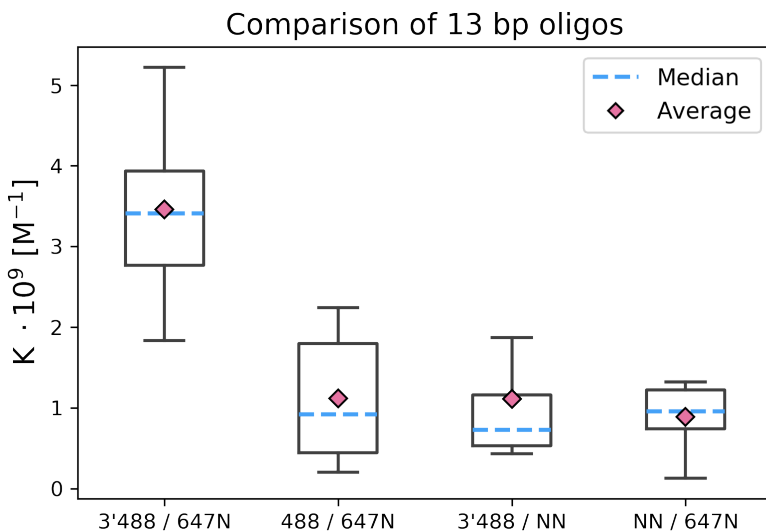


FIGURE 3.16: A comparison of equilibrium constants obtained the from brightness method for all experimental oligonucleotide pairs at 25 °Cin 20 mM PB buffer. Box-whisker plots represent the distributions of equilibrium constants for double-labeled and single labeled pairs. The bottom and top edge of boxes show the first (Q1) and third quartiles (Q3). The whiskers show the minimum and maximal values (excluding outliers). The medians and averages are shown accordingly to the figure legend.

The obtained results from single labeled pairs experiments show the complexity of energy transfer in double-labeled pairs with ATTO488 and ATTO647N dyes. In the double-labeled system, three competing effects overlap. They will be discussed on the example of pair 488/647N (opposite ends). The first effect is directly related to energy transfer according to the FRET theorem. In the close distance (< 10 nm) two fluorophores of specific spectral properties exchange the energy depending on the separating distance between them. The pair 488/647N (opposite ends) ' energy transfer efficiency was 34% upon complex formation. This value describes the situation that for 100 photons absorbed by donor 34 are transferred to the red channel. Figure 3.12b shows the inequality of photons transfer (60 photons decrease in blue, and 290 increase in red channel).

Whereas in the case of brightness analysis upon the hybridization of DNA duplex ATTO488 increases MB by 22% (expected 715 photons according to initial 580). The difference between 715 and observed 520 is 195. After correction

by factor $\eta = 1.38$ this changes to 270 photons. Lastly, 5% decrease of MB by ATTO647N upon hybridization might facilitate energy transfer, which should fills the missing 30 photons. This suggest that additional MB changes by each fluorophore in any double-labeled system for the FRET measurements may affect estimated $FRET_{MAX}$ [82, 151]. Such effects need to be considered during the design and analysis of experiments where FRET is used.

3.3 Factors that affect K : crowded environment and ionic strength

The determination of the equilibrium constant in a simple buffer solution ignores the living organism's internal complexity. The cell's interior is inhomogeneous (in terms of ion distribution) and a heavily crowded environment. Those factors may significantly affect the local environment of substrates and their diffusion within the cell. Often due to the difficulties of conducting research inside the cell or due to low concentration of reagents (e.g., a common expression of a particular protein), tests are carried out *in-vitro*, maintaining the most similar conditions (e.g., in a cell lysate). From the perspective of soft matter studies, research is often carried out with the use of cosolutes (crowding agents) to mimic cell interior. Usually, experiments are carried out to check how crowding molecules of different sizes, chemical structures, and concentrations can influence the reactants' diffusion and reaction kinetics [124, 152–156]. On the other hand concentration of salts regulate the physiological processes of the cell. A significant part of biochemistry is based on reactions where at least one of the reaction components possesses a charge. Such interactions are observed in selected proteins, metabolic-substrates with carboxyl or phosphate group, complex-forming polypeptides(antibodies), DNA or RNA interactions, and membrane building anionic phospholipids with embedded charge proteins. The activity of enzymes or receptors is controlled by forming ion-based complexes with specific cations, e.g., calcium or magnesium. Those types of interactions are greatly responsive to the changes of ions concentration in the solution. The effective ion concentration in the solution is described by ionic strength (IS). The value of IS provides the information that determines the effective electrostatic repulsion distance (Debye length). Partially in the initial part of this dissertation, ionic strength's influence affected the DNA's T_m and K . Aberration of ionic strength impacts kinetics of complex formation, but also a lack of specific ions may also affect substrate structure binding mechanism.

3.3.1 DNA Hybridization in crowded environment

The molecular crowding effect is usually carried out in water/buffer solutions to mimic the living systems' environment. The applied cosolutes are usually hydrophilic and characterized by the presence of the oxygen or nitrogen-containing groups. Residual charge electrons cause those crowders' wettability on those groups that attract water molecules through the Van der Waals interactions. The formation of a double-stranded DNA backbone is an electrostatic interaction between two complementary, negatively-charged strands. The initial task was to monitor the crowded environment's effect on the hybridization of complementary strands in biochemical concentration regimes (around single nM). Using the brightness analysis method, I observed the most popular crowding agents (i.e., glycerol, ethylene glycol, Ficoll, PEG, and dextrans) on DNA hybridization by determining the K value at different concentration of cosolutes. By increase of crowders concentration (regardless of the used cosolute), the K decreases, see Figure 3.17.

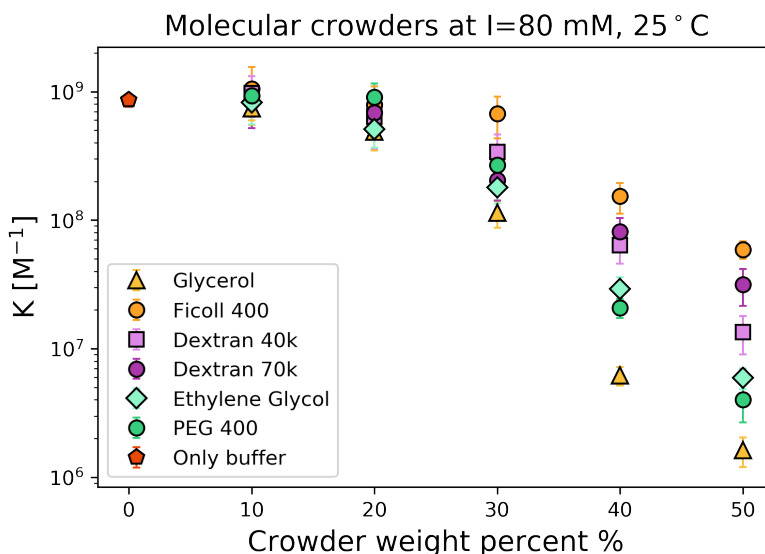


FIGURE 3.17: The hybridization reaction was measured at constant ionic strength in the presence of various crowder agents. The effect of crowder molecules on reaction components (presented in nM concentration) is negligible below few wt.% of crowder concentration (~ 200 mM). The crowders affect reaction when their molar concentration is in \sim few M regime.

The crowding influence the thermodynamic stability of DNA duplexes formation was previously determined in the presence of various crowders [156, 157]. Here, at low crowders concentrations, the decrease is nearly negligible. In higher concentrations, the reduction of K is significant. There is no correlation between the different structure and their sizes of tested cosolutes.

The influence of the crowded environment changes the K by even two to three orders of magnitude for a high concentration of crowders (40 wt.%<). In terms of the molar concentration, this value corresponds to values above 10 M. This means that the crowders are in over 10^9 times fold excess over concentration of substrates in this reaction (~ 1 nM). Hence, if the crowding effect were significant, it would be observable at much lower concentrations. Therefore, the effect responsible for changes of K is not secondary interaction with crowder molecule nor effect caused by depletion with it, but rather some weak effect or interaction.

It was reported that such polymers might, in fact, complex cations suspended in the solvent [158–161]. The reported values for complexation the cations by different PEG molecules are in the range of 10^0 to 10^2 M⁻¹. These values depend on the charge (e.g., Na⁺ or Ca²⁺) and the conjugated acidic residual (strong or weak, e.g., phosphate or acetate) [162, 163].

The concentration of salts regulates the physiological processes of the cell. A significant part of biochemistry is based on reactions where at least one of the reaction components possesses a charge. The changes of ionic strength shift the equilibrium of ion of those biochemical non-covalent complexes, such as complex-forming polypeptides(antibodies), stabilization of membrane building anionic phospholipids, protein-DNA, DNA-drug, metabolic-substrates with carboxyl or phosphate group, etc. Also, enzymes or receptors' activity is controlled by forming ion-based complexes with specific cations to obtain proper active conformation [164–167].

Considering all this, the decrease of the equilibrium constant in a crowded environment (shown in the Figure 3.17) is observed due to ion deficiency caused by complexation of cations in the solution. The decrease of ions concentration in the Debye double layer reduces the screening of negative charges on oligonucleotide backbones. This results in electrostatic repulsion between DNA strands and, finally, the lower bound fraction.

3.3.2 Influence of ionic strength on DNA hybridization

The effective ion concentration in the solution is described by ionic strength (IS), and it determines the effective electrostatic repulsion distance (Debye length). The influence of ionic strength on physico-chemical properties, e.g., the formation of non-covalent complexes or DNA melting temperature, can be predicted. Although, aberration of ionic strength impacts kinetics of DNA complex formation, and thus some models fall behind in providing proper characteristics of the reaction [35].

During the DNA hybridization, the base pair repulsion (caused by phosphodiester groups) is partially neutralized by cations (e.g., Na^+ , K^+ or Mg^{2+}). The hybridization of 13 bp complementary DNA strands was investigated at different ionic strengths (in a range of ~ 100 times lower than physiological concentrations and at a highly saline environment), see Figure 3.18. The experimental PB buffer (where only sodium ions were introduced as positively charged species) was used at various concentrations to obtain different IS. At each IS, using the brightness analysis method, the equilibrium constant K of DNA was determined. The result was also validated on double-labeled pair (3'488/647N).

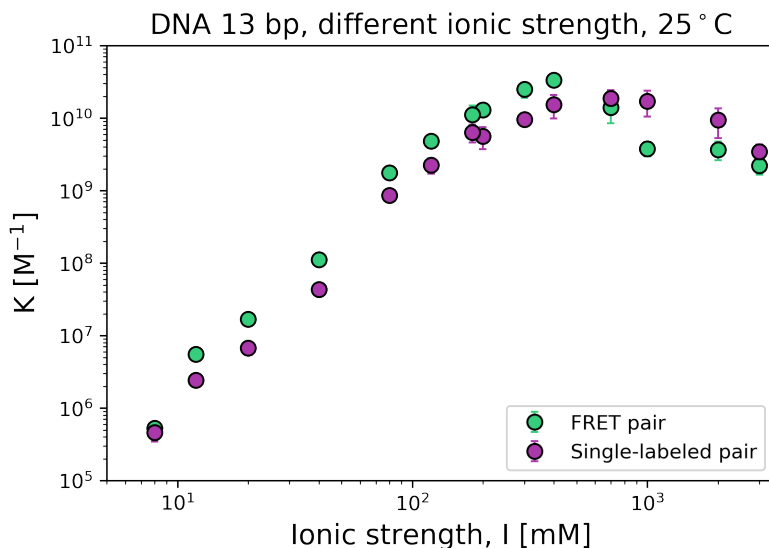


FIGURE 3.18: The influence of ionic strength on the hybridization of complementary DNA oligonucleotide strands.

The increase in ionic strength initially causes a polynomial growth in the constant K in respect to IS, where the maximum value is obtained for 700 mM of ionic strength. The increase in salt concentration changes the binding energy between complementary DNA fragments to a significant extent. The presence of sodium cations and phosphate anions with a total ionic strength of 10 mM generates an increase in the constant K by 10^6 M^{-1} to pure water, where the reaction does not take place (or in other words can be neglected).

The ions in the solution screen the negative charges found on the phosphate groups. Accordingly, the Debye length and the effective negative charge of the oligonucleotides are reduced. Dispersive interactions start to dominate over the repulsive electrostatic forces between DNA strands. As a result, the probability of forming a DNA complex increases. For ionic strength greater than 700 mM, the K constant decreases. This unintuitive deviation is probably caused by the situation when the Debye length is comparable or smaller than the hydrodynamic radius of substrate. A similar effect was observed on the surface coverage with charged nanoparticles at different ionic strengths [168]. At the 2 M ionic strength, the DNA double-strand formation constant value is 10 times lower than the maximum value observed. In this regime, the oligonucleotides' charge is most strongly screened. Thus the repulsive electrostatic interactions between single DNA strands can be completely ignored.

3.3.3 Complexation of sodium ions by crowders

The decrease of ions concentration in the Debye double layer reduces the screening of negative charges on oligonucleotide backbones. This results in electrostatic repulsion between DNA strands and, thus, the lower bound fraction, see Figure 3.19. The interaction mechanism of ion complexation by different crowders is presented schematically in Equation 3.10. The binding site for cation within crowder structure may differ even between crowders of the same binding moiety (functional group), i.e., polyethylene glycol and ethylene glycol. Therefore, the interaction with the given crowder is calculated per molecule or monomer (in the case of polymers).



The equilibrium constant for this interaction can be written as:

$$\kappa = \frac{[\text{Na} \cdot \text{CW}]^{eq}}{[\text{Na}^+]^{eq} \cdot [\text{CW}]^{eq}} = \frac{[\text{Na} \cdot \text{CW}]^{eq}}{([\text{Na}^+]^0 - [\text{Na} \cdot \text{CW}]^{eq}) \cdot ([\text{CW}]^0 - [\text{Na} \cdot \text{CW}]^{eq})}$$
(3.11)

where, $[\text{Na}^+]^0$ and $[\text{CW}]^0$ are initial molar concentration of sodium ions and crowder molecules, respectively.

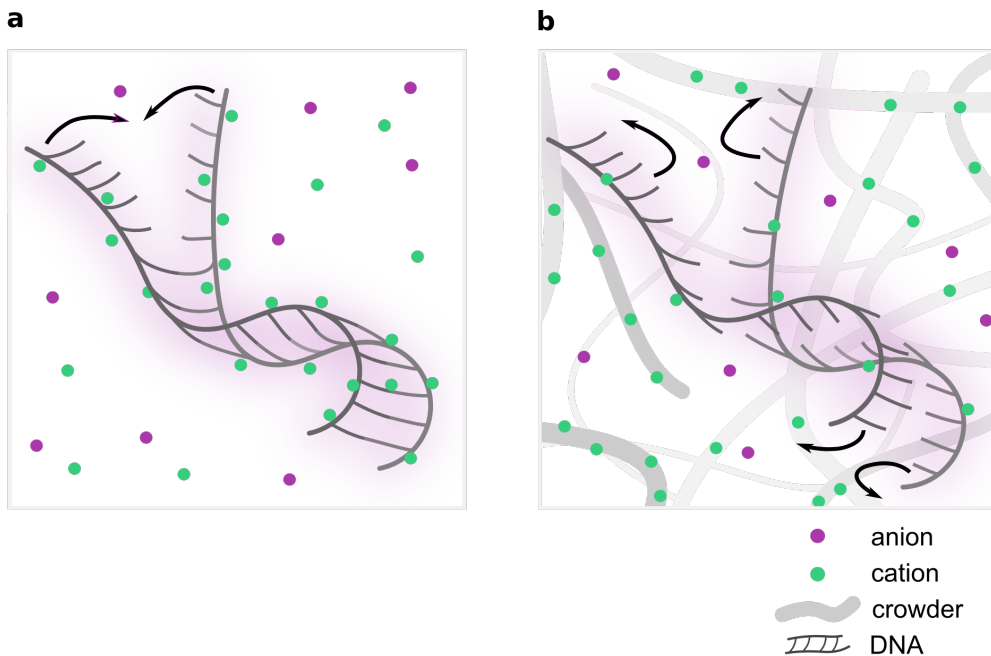


FIGURE 3.19: The scheme of ion complexation mechanism by highly crowded environment. **a** Sodium cations screen negative charge of DNA backbone, which facilitates the complex formation. **b** After addition of crowders, sodium cations are getting complexed by weak interaction with crowder molecules. In high concentration of crowders, repulsion of the DNA strands became to be more pronounced due to reduction of screening charges on the DNA backbone.

Following the brightness analysis method to estimate the ion complexation by crowders, in the measurements, the prepared buffer includes only sodium cations, Na^+ . The method of buffer preparation enables to keep the

pH constant even at different ionic strengths. The influence of different crowders on pH was investigated, see Figure 3.20a. The concentration of crowders was set to 40 wt.% to verify possible changes to the hybridization. The K of DNA hybridization was then estimated in a pH range from 6.5 up to 8. No significant difference was observed, Figure 3.20b.

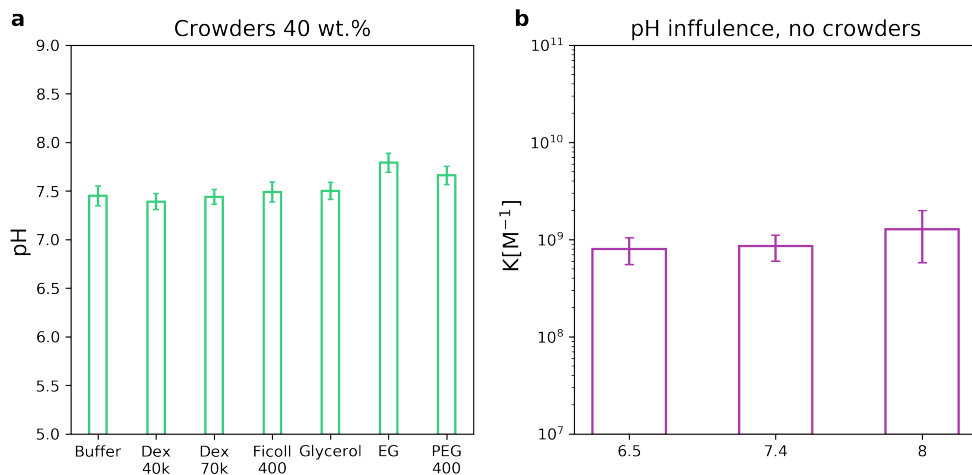


FIGURE 3.20: Influence of the presence of crowders on the pH of the system. **a** The measurement was made in a high concentration of crowders with constant ionic strength buffers (20 mM). **b** Effect of pH change on hybridization without crowders in the constant ionic strength of the reaction buffer (20 mM).

Determination of ion complexation constant, κ was prepared as follows:

- The DNA hybridization constant, K (without any crowder) was an indicator of sodium concentration, see violet points in Figure 3.21a. The obtained results were fitted by function, $K = A \cdot [Na^+]^B$, where $A=5.5 \cdot 10^{12}$ and $B=2.42$.
- The K were determined in series where **crowders concentration was set constant**, but ionic strength was varied (green points). The obtained K values were transformed according to the function $K = A \cdot [Na^+]^B$.
- The difference between K values obtained in experiment with and without cosolute corresponds to the concentration of complexed sodium ions by crowder molecule, $[Na \cdot CW]^{eq}$ according to Equation 3.10.

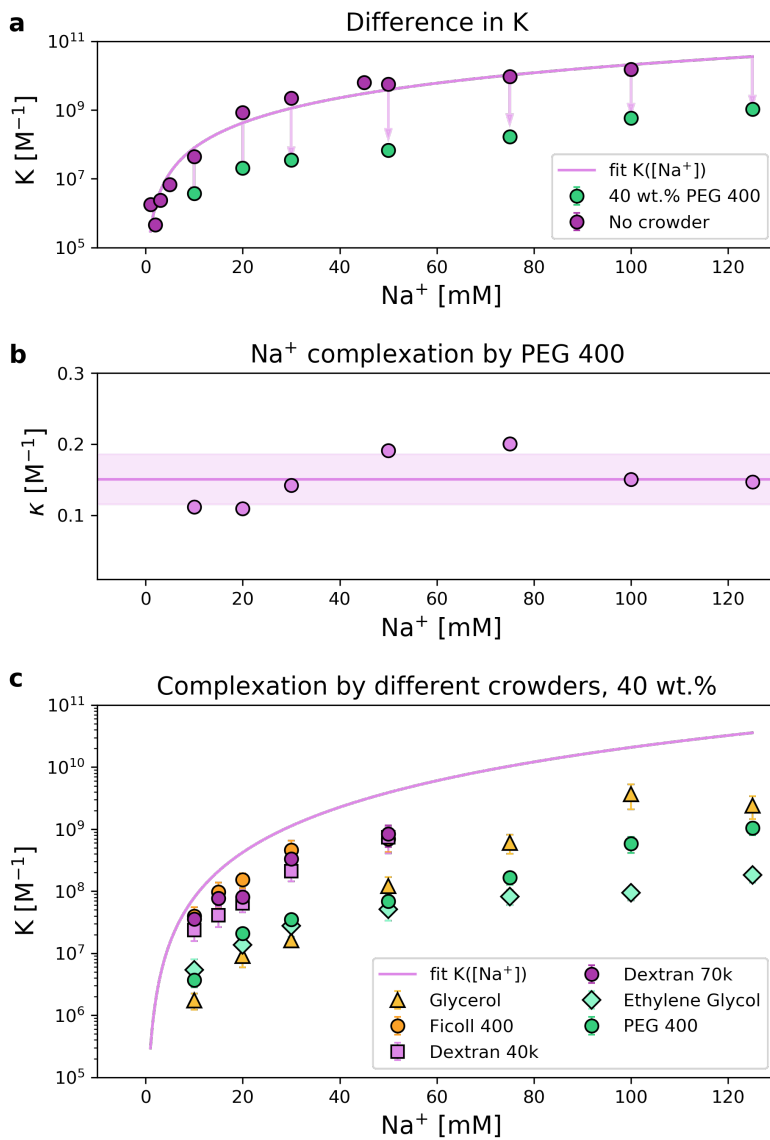


FIGURE 3.21: **a** The hybridization constant depending on the concentration of sodium ions without the addition of cosolute (violet dots) and in the presence of 40 wt.% PEG 400 (green dots). The arrows in the plot correspond to the difference between the K values, thus reducing complexed sodium cations. **b** The constant of sodium ion complexation by PEG 400 at various concentrations of sodium cations in the solution. The violet line represents the average value of the constant κ determined per one PEG 400 monomer. Based on those results, the complexation of sodium ions by crowders, but not their direct interactions with substrates, is mostly responsible for the changes in equilibrium constants. **c** The results obtained for all the crowding agents considered in this work.

Such an approach is presented in Figure 3.21a, where PEG of average molecular weight 400 Da (PEG400) was used as a crowder agent. Following the Equation 3.11 ion complexation equilibrium constant, κ , was determined and averaged it over series of data points, see Figure 3.21b. This methodology was performed over the most popular crowding agents used in biochemical experiments. Crowders were differentiated in molecular sizes and chemical structure (only oxygen was used as a heteroatom in functional groups). The differences in K compared to the function obtained in non-crowded environment are presented in Figure 3.21c. The difference in size is not pronounced, especially in crowders similar in structure (sugar moiety), e.g., big dextran of average molecular weight 70 kDa and small ficoll, ~400 Da. The determined κ values calculated per crowder molecule or monomer (in the case of polymers) are summarized in Figure 3.22.

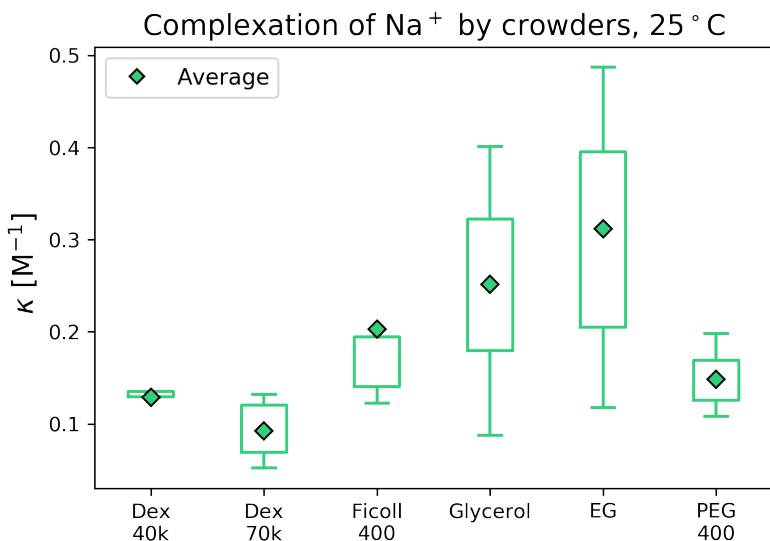


FIGURE 3.22: Comparison of determined sodium complexation equilibrium constant by different crowders.

The obtained approach covers the application of crowders different in sizes and structures. However, the cation complexation capability strength is similar in value (and order of magnitude) among all presented cosolutes. Observed reaction (hybridization of DNA) is a perfect example of reactions of formation of non-covalent complexes which kinetics are sensitive for changes

in ionic strength. The changes of ionic Debye layer determines the screening of electrostatic interaction between substrates of the reaction, and thus the formation of a complex. Performing a reaction in a crowded environment without considering the interaction with ions may lead to inconclusive research results, especially in *in-vitro* experiments. On the other hand, the deficiency or excess of ions in living systems is regulated through osmosis or active transport. Thus, for example, the polymer nanoprobes within living cells should not affect internal ionic strength. Observed interaction is very weak and can be neglected in an environment where crowder concentration is below 1 wt.% or, e.g., when reaction occurs in polymer containers.

Although, crowders' influence is related to the effect on ionic strength and the direct impact on the substrates of reaction. It was shown that the presence of the crowder molecule near the local neighborhood of the protein substrate might affect its dielectric properties and its hydration structure [169]. Additionally, additional experiments are required to approximate the direct effect of repulsive forces between Reactants and crowder shells. To extract this information, the experiment should be carried out on a series that consists of a broad molecular weight range of the same type of molecule (e.g., for PEG from 200 Da to 50 kDa). In such a designed system, it is possible to obtain the dependence of the strength of interaction between substrates as a function of the hydrodynamic radius of the crowder molecule [125].

Chapter 4

Summary and Conclusions

The **main achievement of this dissertation** is development of the **molecular brightness analysis** as a method for determination of equilibrium constant of complex formation ($A + B \rightleftharpoons AB$). The **major advantage of the brightness analysis** is that to operate it **uses only one fluorescent substrate** instead of two (as in the FRET case). Thus, results obtained by brightness analysis were validated by FRET. The method relies on the changes of molecular brightness of a fluorophore upon the complex formation. The K can be obtained at nanomolar and subnanomolar concentrations, for molecular brightness changes as low as 5% irrespective of the direction of change (increase or decrease of molecular brightness).

The **initial part** focuses on applying the FRET method to determine K and kinetics at extremely low concentrations approaching 10 pM. I showed that DNA oligonucleotide binding and dissociation kinetics **are unexpectedly slow at subnanomolar concentrations** and in low ionic strength conditions. At such conditions establishing equilibrium may take several days. Neglecting the time required to reach the equilibrium as a factor while designing experiments may result in immense errors in the observed results. The issue is crucial in any single-molecule experimental approach.

The equilibrium and kinetic constants were measured for hybridization and melting of DNA oligonucleotides of a length of 10, 13, and 20 bases, at three different temperatures and in phosphate buffer at two ionic strengths. Experiments covered a wide range of oligonucleotide concentrations from 10 pM to 100 μ M. According to Arrhenius law, the results show that at low ionic

strength binding and unbinding of the DNA strands are processes of positive activation energy, both above and below the melting temperature.

The effect of rebinding (the same pair of substrates molecules reacts and dissociates multiple times in a short time) at low concentrations on K was investigated by Reaction-diffusion molecular simulations. The results show that the association and dissociation rates are intrinsically normalized by fast re-binding after dissolution. Thus, a single value of K is independent of reagent concentrations even at picomolar concentrations. However approaching equilibrium is extremely slow.

In FRET analysis, there is a discrepancy in the number of photons emitted by both substrates before and after complex formation. Those discrepancies are not caused by resonant energy transfer. The difference can be corrected by performing two experiments separately, where donor and acceptor labeled substrate is mixed with a corresponding non-labeled substrate. Observed photophysical changes were the basis of research on the development of the brightness analysis method.

The **application of the method** was demonstrated on DNA complementary pairs separately labeled with commercially available ATTO488 and ATTO647N dyes. Those dyes changed brightness upon DNA hybridization sufficiently **to determine K, and thus the strength of interactions**. In case of ATTO488 dye the effect **allowed K determination at picomolar concentration regime**. Whereas in the case of ATTO647N, reproducible results are obtainable just by **molecular brightness changes as low as 5%** concerning the initial value.

The values of K estimated on the same pairs obtained by FRET and brightness method show no significant differences. The recent application example of this method showed the determination of interaction between DNA and anticancer drug family – anthracyclines. In this system, molecular brightness is enabled to provide an insight into the reaction mechanism [8]. It is expected that **brightness method can be enhanced by synthesizing novel fluorophores with higher sensitivity** as well as by **adapting it to any microscope system including super resolution techniques i.e. TIRF or STED**.

Lastly, the brightness analysis method **was used to investigate** two factors that affect non-covalent complex formation: **crowded environment** and **ionic strength**. The strength of interactions between substrates increases as the ionic strength is increased. Although, after exceeding the specific value, ionic strength augmented the reducing effect on the bound fraction, which is unintuitive at first sight. This observation may be crucial for further analysis of organisms' biochemical reactions in a highly saline environment or with less access to water.

The further experiments performed in the crowded environment employed the hybridization of DNA reaction as an indicator of sodium ions concentration. **The results showed that ions complexation, but not molecular crowding** might be responsible for most **changes in equilibrium constants of DNA hybridization**. Ion complexation for most popular crowders (differentiated in sizes and chemical structure) is considerably low and negligible in most experiments (on average constant $\kappa \sim 0.2 \text{ M}^{-1}$). Nevertheless, a used approximation can not neglect the impact of excluded volume or direct interactions with cosolute molecules to describe energies distribution presented in a crowded environment.

Bibliography

- (1) Smith, J.; Andes, D. *Therapeutic drug monitoring* **2008**, *30*, 167–172.
- (2) Csermely, P.; Agoston, V.; Pongor, S. *Trends in pharmacological sciences* **2005**, *26*, 178–182.
- (3) Wan, X.; Zhang, W.; Li, L.; Xie, Y.; Li, W.; Huang, N. *Journal of medicinal chemistry* **2013**, *56*, 2619–2629.
- (4) Kerwin, S. M. *Current pharmaceutical design* **2000**, *6*, 441–471.
- (5) Mittal, N. *PloS one* **2012**, *7*, e51796.
- (6) Traut, T. W. *Molecular and cellular biochemistry* **1994**, *140*, 1–22.
- (7) Bubak, G.; Kwapiszewska, K.; Kalwarczyk, T.; Bielec, K.; Andryszewski, T.; Iwan, M.; Bubak, S.; Hołyst, R. *The Journal of Physical Chemistry Letters* **2020**, *12*, 294–301.
- (8) Zhou, Y.; Bielec, K.; Pasitsuparoad, P.; Hołyst, R. *Analyst* **2020**.
- (9) Perez-Arnaiz, C.; Bustó, N.; Leal, J. M.; García, B. *The Journal of Physical Chemistry B* **2014**, *118*, 1288–1295.
- (10) Vamathevan, J.; Clark, D.; Czodrowski, P.; Dunham, I.; Ferran, E.; Lee, G.; Li, B.; Madabhushi, A.; Shah, P.; Spitzer, M., et al. *Nature Reviews Drug Discovery* **2019**, *18*, 463–477.
- (11) Schneider, G. *Nature reviews drug discovery* **2018**, *17*, 97.
- (12) Hughes, J. P.; Rees, S.; Kalindjian, S. B.; Philpott, K. L. *British journal of pharmacology* **2011**, *162*, 1239–1249.
- (13) Drews, J. *science* **2000**, *287*, 1960–1964.

- (14) Matej Mikulic, s. Pharmaceuticals: cost of drug development in the U.S. since 1975 <https://www.statista.com/statistics/265054/pharmaceuticals-cost-of-development-in-the-us/> (accessed 01/25/2021).
- (15) Xue, H.; Li, J.; Xie, H.; Wang, Y. *International journal of biological sciences* **2018**, *14*, 1232.
- (16) Prasad, V.; Mailankody, S. *JAMA internal medicine* **2017**, *177*, 1569–1575.
- (17) Yuan, S.; Yu, B.; Liu, H.-M. *European Journal of Medicinal Chemistry* **2020**, *112667*.
- (18) Borlongan, C. V. *Stem cells translational medicine* **2019**, *8*, 983–988.
- (19) Gee, A. P. *Molecular Therapy* **2013**, *21*, 1639–1640.
- (20) Täubel, J.; Hauke, W.; Rump, S.; Viereck, J.; Batkai, S.; Poetzsch, J.; Rode, L.; Weigt, H.; Genschel, C.; Lorch, U., et al. *European Heart Journal* **2021**, *42*, 178–188.
- (21) Emily Capra, J. S.; Guang Yang, m. Gene therapy coming of age: Opportunities and challenges to getting ahead <https://www.mckinsey.com/industries/pharmaceuticals-and-medical-products/our-insights/gene-therapy-coming-of-age-opportunities-and-challenges-to-getting-ahead#> (accessed 01/25/2021).
- (22) Terry, M. A Look at the Top 20 Most Expensive Drugs in the U.S. <https://www.biospace.com/article/-most-expensive-drugs-in-the-u-s-the-top-20/> (accessed 01/25/2021).
- (23) Keeler, A. M.; Flotte, T. R. *Annual review of virology* **2019**, *6*, 601–621.
- (24) Finkel, R. S.; Mercuri, E.; Darras, B. T.; Connolly, A. M.; Kuntz, N. L.; Kirschner, J.; Chiriboga, C. A.; Saito, K.; Servais, L.; Tizzano, E., et al. *N Engl J Med* **2017**, *377*, 1723–1732.
- (25) Russell, S.; Bennett, J.; Wellman, J. A.; Chung, D. C.; Yu, Z.-F.; Tillman, A.; Wittes, J.; Pappas, J.; Elci, O.; McCague, S., et al. *The Lancet* **2017**, *390*, 849–860.

- (26) Diaz, G. A.; Schulze, A.; Longo, N.; Rhead, W.; Feigenbaum, A.; Wong, D.; Merritt II, J. L.; Berquist, W.; Gallagher, R. C.; Bartholomew, D., et al. *Molecular genetics and metabolism* **2019**, *127*, 336–345.
- (27) Kellett, A.; Molphy, Z.; Slator, C.; McKee, V.; Farrell, N. P. *Chemical Society Reviews* **2019**, *48*, 971–988.
- (28) Coelho, M.; Maghelli, N.; Tolić-Nørrelykke, I. M. *Integrative Biology* **2013**, *5*, 748–758.
- (29) Pfeiffer, T.; Poll, S.; Bancelin, S.; Angibaud, J.; Inavalli, V. K.; Keppler, K.; Mittag, M.; Fuhrmann, M.; Nägerl, U. V. *Elife* **2018**, *7*, e34700.
- (30) Kwapiszewska, K.; Kalwarczyk, T.; Michalska, B.; Szczepański, K.; Szymański, J.; Patalas-Krawczyk, P.; Andryszewski, T.; Iwan, M.; Duszyński, J.; Hołyst, R. *Scientific reports* **2019**, *9*, 1–9.
- (31) Carson, E. M.; Watson, J. R. *University Chemistry Education* **2002**, *6*, 4–12.
- (32) Hołyst, R.; Poniewierski, A., *Thermodynamics for chemists, physicists and engineers*; Springer Science & Business Media: 2012.
- (33) Halliday, D.; Resnick, R.; Walker, J., *Fundamentals of physics*; John Wiley & Sons: 2013.
- (34) Hu, C.-D.; Chinenov, Y.; Kerppola, T. K. *Molecular cell* **2002**, *9*, 789–798.
- (35) Bielec, K.; Sozanski, K.; Seynen, M.; Dziekan, Z.; ten Wolde, P. R.; Hołyst, R. *Physical Chemistry Chemical Physics* **2019**, *21*, 10798–10807.
- (36) Van Rood, J. v.; Van Leeuwen, A.; Ploem, J. *Nature* **1976**, *262*, 795.
- (37) Gilli, P.; Ferretti, V.; Gilli, G.; Borea, P. A. *The Journal of Physical Chemistry* **1994**, *98*, 1515–1518.
- (38) De Lean, A.; Stadel, J.; Lefkowitz, R. *Journal of Biological Chemistry* **1980**, *255*, 7108–7117.
- (39) Lu, H.; Tonge, P. J. *Current opinion in chemical biology* **2010**, *14*, 467–474.
- (40) Rehman, S. U.; Sarwar, T.; Husain, M. A.; Ishqi, H. M.; Tabish, M. *Archives of biochemistry and biophysics* **2015**, *576*, 49–60.
- (41) Fielding, L. *Current topics in medicinal chemistry* **2003**, *3*, 39–53.

- (42) Garbett, N. C.; Ragazzon, P. A.; Chaires, J. B. *Nature Protocols* **2007**, *2*, 3166.
- (43) Jelesarov, I.; Bosshard, H. R. *Journal of molecular recognition* **1999**, *12*, 3–18.
- (44) Olaru, A.; Bala, C.; Jaffrezic-Renault, N.; Aboul-Enein, H. Y. *Critical reviews in analytical chemistry* **2015**, *45*, 97–105.
- (45) Liu, Y.; Yu, X.; Zhao, R.; Shangguan, D.-H.; Bo, Z.; Liu, G. *Biosensors and Bioelectronics* **2003**, *18*, 1419–1427.
- (46) Rao, B.; Buttlare, D.; Cohn, M. *Journal of Biological Chemistry* **1976**, *251*, 6981–6986.
- (47) Lakowicz, J. R., *Principles of fluorescence spectroscopy*; Springer science & business media: 2013.
- (48) Markvart, T. *Journal of Physics C: Solid State Physics* **1981**, *14*, L895.
- (49) Schulman, S. G., *Fluorescence and phosphorescence spectroscopy: physico-chemical principles and practice*; Elsevier: 2017.
- (50) Bielec, K.; Bubak, G.; Kalwarczyk, T.; Holyst, R. *Journal of Physical Chemistry B* **2020**, *124*, 1941–1948.
- (51) Suhling, K.; French, P. M.; Phillips, D. *Photochemical & Photobiological Sciences* **2005**, *4*, 13–22.
- (52) Tsien, R. Y. *Annual review of biochemistry* **1998**, *67*, 509–544.
- (53) Mitra, R. D.; Silva, C. M.; Youvan, D. C. *Gene* **1996**, *173*, 13–17.
- (54) Robbins, M. A., *The collector's book of fluorescent minerals*; Springer Science & Business Media: 2013.
- (55) Lichtman, J. W.; Conchello, J.-A. *Nature methods* **2005**, *2*, 910–919.
- (56) Huang, B.; Bates, M.; Zhuang, X. *Annual review of biochemistry* **2009**, *78*, 993–1016.
- (57) Vicedomini, G.; Bianchini, P.; Diaspro, A. *Nature methods* **2018**, *15*, 173.
- (58) Axelrod, D. *Methods in cell biology* **1989**, *30*, 245–270.
- (59) Pohl, D. W.; Denk, W.; Lanz, M. *Applied physics letters* **1984**, *44*, 651–653.

- (60) Lewis, A.; Isaacson, M.; Harootunian, A.; Muray, A. *Ultramicroscopy* **1984**, *13*, 227–231.
- (61) Nwaneshiudu, A.; Kuschal, C.; Sakamoto, F. H.; Anderson, R. R.; Schwarzenberger, K.; Young, R. C. *Journal of Investigative Dermatology* **2012**, *132*, 1–5.
- (62) Suzuki, T.; Fujikura, K.; Higashiyama, T.; Takata, K. *Journal of Histochemistry & Cytochemistry* **1997**, *45*, 49–53.
- (63) Wilson, T. In *Handbook of biological confocal microscopy*; Springer: 1995, pp 167–182.
- (64) Frach, T.; Prescher, G.; Degenhardt, C.; De Gruyter, R.; Schmitz, A.; Ballizany, R. In *2009 IEEE Nuclear Science Symposium Conference Record (NSS/MIC)*, 2009, pp 1959–1965.
- (65) Zappa, F.; Tisa, S.; Tosi, A.; Cova, S. *Sensors and Actuators A: Physical* **2007**, *140*, 103–112.
- (66) Elson, E. L.; Magde, D. *Biopolymers: Original Research on Biomolecules* **1974**, *13*, 1–27.
- (67) Hess, S. T.; Webb, W. W. *Biophysical journal* **2002**, *83*, 2300–2317.
- (68) Rigler, R.; Elson, E. S., *Fluorescence correlation spectroscopy: theory and applications*; Springer Science & Business Media: 2012; Vol. 65.
- (69) Haustein, E.; Schwille, P. *Annu. Rev. Biophys. Biomol. Struct.* **2007**, *36*, 151–169.
- (70) Holyst, R.; Bielejewska, A.; Szymański, J.; Wilk, A.; Patkowski, A.; Gapiński, J.; Żywociński, A.; Kalwarczyk, T.; Kalwarczyk, E.; Tabaka, M., et al. *Physical Chemistry Chemical Physics* **2009**, *11*, 9025–9032.
- (71) Uhlenbeck, G. E.; Ornstein, L. S. *Physical review* **1930**, *36*, 823.
- (72) Zhang, X.; Poniewierski, A.; Jelińska, A.; Zagoźdżon, A.; Wisniewska, A.; Hou, S.; Hołyst, R. *Soft Matter* **2016**, *12*, 8186–8194.
- (73) Zhang, X.; Poniewierski, A.; Sozański, K.; Zhou, Y.; Brzozowska-Elliott, A.; Holyst, R. *Physical Chemistry Chemical Physics* **2019**, *21*, 1572–1577.

- (74) Piston, D. W.; Kremers, G.-J. *Trends in biochemical sciences* **2007**, *32*, 407–414.
- (75) Medintz, I. L.; Hildebrandt, N., *FRET-Förster resonance energy transfer: from theory to applications*; John Wiley & Sons: 2013.
- (76) Didenko, V. V. *Biotechniques* **2001**, *31*, 1106–1121.
- (77) Phillip, Y.; Kiss, V.; Schreiber, G. *Proceedings of the National Academy of Sciences* **2012**, *109*, 1461–1466.
- (78) Loura, L. *International journal of molecular sciences* **2012**, *13*, 15252–15270.
- (79) Cao, L.; Cheng, L.; Zhang, Z.; Wang, Y.; Zhang, X.; Chen, H.; Liu, B.; Zhang, S.; Kong, J. *Lab on a Chip* **2012**, *12*, 4864–4869.
- (80) Zhang, C.-y.; Johnson, L. W. *Angewandte Chemie International Edition* **2007**, *46*, 3482–3485.
- (81) Bhuckory, S.; Kays, J. C.; Dennis, A. M. *Biosensors* **2019**, *9*, 76.
- (82) Roy, R.; Hohng, S.; Ha, T. *Nature methods* **2008**, *5*, 507.
- (83) Bielec, K.; Bubak, G.; Kalwarczyk, T.; Holyst, R. *The Journal of Physical Chemistry B* **2020**, *124*, 1941–1948.
- (84) Alberts, B.; Bray, D.; Hopkin, K.; Johnson, A. D.; Lewis, J.; Raff, M.; Roberts, K.; Walter, P., *Essential cell biology*; Garland Science: 2015.
- (85) Alberts, B.; Johnson, A.; Lewis, J.; Morgan, D.; Raff, M.; Roberts, K.; Walter, P., *Molecular Biology of the Cell, Sixth Edition*; Taylor & Francis Group: 2014.
- (86) Davis, L., *Basic Methods in Molecular Biology*; Elsevier Science: 2012.
- (87) Arboleda, V. A.; Xian, R. R. *Biobanking* **2019**, 385–402.
- (88) Nyce, J. W.; Metzger, W. J. *Nature* **1997**, *385*, 721.
- (89) Tamm, I.; Dörken, B.; Hartmann, G. *The Lancet* **2001**, *358*, 489–497.
- (90) Donnelly, C. J.; Zhang, P.-W.; Pham, J. T.; Haeusler, A. R.; Mistry, N. A.; Vidensky, S.; Daley, E. L.; Poth, E. M.; Hoover, B.; Fines, D. M., et al. *Neuron* **2013**, *80*, 415–428.

- (91) Martinovich, K. M.; Shaw, N. C.; Kicic, A.; Schultz, A.; Fletcher, S.; Wilton, S. D.; Stick, S. M. *Molecular and cellular pediatrics* **2018**, *5*, 3.
- (92) Rothmund, P. W. *Nature* **2006**, *440*, 297.
- (93) Wang, K.; Tang, Z.; Yang, C. J.; Kim, Y.; Fang, X.; Li, W.; Wu, Y.; Medley, C. D.; Cao, Z.; Li, J., et al. *Angewandte Chemie International Edition* **2009**, *48*, 856–870.
- (94) Owczarzy, R.; Dunietz, I.; Behlke, M. A.; Klotz, I. M.; Walder, J. A. *Proceedings of the National Academy of Sciences* **2003**, *100*, 14840–14845.
- (95) Meinkoth, J.; Wahl, G. *Analytical biochemistry* **1984**, *138*, 267–284.
- (96) Breslauer, K. J.; Frank, R.; Blöcker, H.; Marky, L. A. *Proceedings of the National Academy of Sciences* **1986**, *83*, 3746–3750.
- (97) Nakano, S.-i.; Fujimoto, M.; Hara, H.; Sugimoto, N. *Nucleic acids research* **1999**, *27*, 2957–2965.
- (98) Zuker, M. *Nucleic acids research* **2003**, *31*, 3406–3415.
- (99) Kibbe, W. A. *Nucleic acids research* **2007**, *35*, W43–W46.
- (100) DeVoe, H.; Tinoco Jr, I. *Journal of molecular biology* **1962**, *4*, 500–517.
- (101) Crothers, D. M.; Zimm, B. H. *Journal of molecular biology* **1964**, *9*, 1–9.
- (102) Sugimoto, N.; Nakano, S.-i.; Yoneyama, M.; Honda, K.-i. *Nucleic acids research* **1996**, *24*, 4501–4505.
- (103) Xia, T.; SantaLucia Jr, J.; Burkard, M. E.; Kierzek, R.; Schroeder, S. J.; Jiao, X.; Cox, C.; Turner, D. H. *Biochemistry* **1998**, *37*, 14719–14735.
- (104) SantaLucia, J. *Proceedings of the National Academy of Sciences* **1998**, *95*, 1460–1465.
- (105) Sikorav, J.-L.; Orland, H.; Braslav, A. *The Journal of Physical Chemistry B* **2009**, *113*, 3715–3725.
- (106) Ouldridge, T. E.; Šulc, P.; Romano, F.; Doye, J. P.; Louis, A. A. *Nucleic acids research* **2013**, *41*, 8886–8895.
- (107) Marimuthu, K.; Chakrabarti, R. *The Journal of chemical physics* **2014**, *140*, 05B605_1.

- (108) Hinckley, D. M.; Lequieu, J. P.; De Pablo, J. J. *The Journal of chemical physics* **2014**, *141*, 07B613_1.
- (109) Gao, Y.; Wolf, L. K.; Georgiadis, R. M. *Nucleic acids research* **2006**, *34*, 3370–3377.
- (110) Chen, C.; Wang, W.; Wang, Z.; Wei, F.; Zhao, X. S. *Nucleic acids research* **2007**, *35*, 2875–2884.
- (111) Flamm, C.; Hofacker, I. L. *Monatshefte für Chemie-Chemical Monthly* **2008**, *139*, 447–457.
- (112) Bonnet, G.; Krichevsky, O.; Libchaber, A. *Proceedings of the National Academy of Sciences* **1998**, *95*, 8602–8606.
- (113) Wallace, M. I.; Ying, L.; Balasubramanian, S.; Klenerman, D. *Proceedings of the National Academy of Sciences* **2001**, *98*, 5584–5589.
- (114) Kim, J.; Doose, S.; Neuweiler, H.; Sauer, M. *Nucleic acids research* **2006**, *34*, 2516–2527.
- (115) Tsukanov, R.; Tomov, T. E.; Masoud, R.; Drory, H.; Plavner, N.; Liber, M.; Nir, E. *The Journal of Physical Chemistry B* **2013**, *117*, 11932–11942.
- (116) Zhang, D. Y.; Winfree, E. *Journal of the American Chemical Society* **2009**, *131*, 17303–17314.
- (117) Tsvetanova, N. G.; Irannejad, R.; von Zastrow, M. *Journal of Biological Chemistry* **2015**, *290*, 6689–6696.
- (118) Ellis, R. J.; Minton, A. P. *Nature* **2003**, *425*, 27–28.
- (119) Sasahara, K.; McPhie, P.; Minton, A. P. *Journal of molecular biology* **2003**, *326*, 1227–1237.
- (120) Tokuriki, N.; Kinjo, M.; Negi, S.; Hoshino, M.; Goto, Y.; Urabe, I.; Yomo, T. *Protein Science* **2004**, *13*, 125–133.
- (121) Luby-Phelps, K. *Molecular biology of the cell* **2013**, *24*, 2593–2596.
- (122) Ridgway, D.; Broderick, G.; Lopez-Campistrous, A.; Ru'aini, M.; Winter, P.; Hamilton, M.; Boulanger, P.; Kovalenko, A.; Ellison, M. J. *Bioophysical journal* **2008**, *94*, 3748–3759.
- (123) Sozański, K.; Ruhnau, F.; Wiśniewska, A.; Tabaka, M.; Diez, S.; Hołyst, R. *Physical review letters* **2015**, *115*, 218102.

- (124) Kalwarczyk, T.; Ziebach, N.; Bielejewska, A.; Zaboklicka, E.; Koynov, K.; Szymanski, J.; Wilk, A.; Patkowski, A.; Gapinski, J.; Butt, H.-J., et al. *Nano letters* **2011**, *11*, 2157–2163.
- (125) Tabaka, M.; Sun, L.; Kalwarczyk, T.; Hołyst, R. *Soft Matter* **2013**, *9*, 4386–4389.
- (126) Chandradoss, S. D.; Haagsma, A. C.; Lee, Y. K.; Hwang, J.-H.; Nam, J.-M.; Joo, C. *Journal of visualized experiments: JoVE* **2014**, *86*, e50549.
- (127) Anaconda Software Distribution, version 2-2.4.0, 2020.
- (128) Virtanen, P. et al. *Nature Methods* **2020**, *17*, 261–272.
- (129) Harris, C. R. et al. *Nature* **2020**, *585*, 357–362.
- (130) Pandas development team, T. *pandas-dev/pandas: Pandas*, version 1.2.1, 2021.
- (131) Hunter, J. D. *Computing in Science & Engineering* **2007**, *9*, 90–95.
- (132) Tabaka, M.; Burdzy, K.; Hołyst, R. *Physical Review E* **2015**, *92*, 022721.
- (133) Smoluchowski, M. v. *Zeitschrift für physikalische Chemie* **1918**, *92*, 129–168.
- (134) Takahashi, K.; Tănase-Nicola, S.; Ten Wolde, P. R. *Proceedings of the National Academy of Sciences* **2010**, *107*, 2473–2478.
- (135) Kempe, D.; Cerminara, M.; Poblete, S.; Schöne, A.; Gabba, M.; Fitter, J. *Analytical Chemistry* **2017**, *89*, 694–702.
- (136) Kalinin, S.; Peulen, T.; Sindbert, S.; Rothwell, P. J.; Berger, S.; Restle, T.; Goody, R. S.; Gohlke, H.; Seidel, C. A. *Nature methods* **2012**, *9*, 1218.
- (137) Bloomfield, V.; Crothers, D.; Tinoco Jr, I. *University Science Books* **2000**, 794.
- (138) Alberty, R. A.; Hammes, G. G. *The Journal of Physical Chemistry* **1958**, *62*, 154–159.
- (139) Van Zon, J. S.; Ten Wolde, P. R. *Physical review letters* **2005**, *94*, 128103.
- (140) Sokolowski, T. R.; Paijmans, J.; Bossen, L.; Miedema, T.; Wehrens, M.; Becker, N. B.; Kaizu, K.; Takahashi, K.; Dogterom, M.; ten Wolde, P. R. *The Journal of chemical physics* **2019**, *150*, 054108.

- (141) Kaizu, K.; De Ronde, W.; Paijmans, J.; Takahashi, K.; Tostevin, F.; Ten Wolde, P. R. *Biophysical journal* **2014**, *106*, 976–985.
- (142) Pörschke, D.; Uhlenbeck, O.; Martin, F. *Biopolymers: Original Research on Biomolecules* **1973**, *12*, 1313–1335.
- (143) Rachofsky, E. L.; Osman, R.; Ross, J. A. *Biochemistry* **2001**, *40*, 946–956.
- (144) Dos Remedios, C. G.; Moens, P. D. *Journal of structural biology* **1995**, *115*, 175–185.
- (145) Marras, S. A.; Kramer, F. R.; Tyagi, S. *Nucleic acids research* **2002**, *30*, e122–e122.
- (146) Minta, A.; Kao, J.; Tsien, R. Y. *Journal of Biological Chemistry* **1989**, *264*, 8171–8178.
- (147) Matta, C. F.; Castillo, N.; Boyd, R. J. *The Journal of Physical Chemistry B* **2006**, *110*, 563–578.
- (148) Wang, L.; Pyle, J. R.; Cimatu, K. L.; Chen, J. *Journal of Photochemistry and Photobiology A: Chemistry* **2018**, *367*, 411–419.
- (149) Dragan, A.; Pavlovic, R.; McGivney, J.; Casas-Finet, J.; Bishop, E.; Strouse, R.; Schenerman, M.; Geddes, C. *Journal of fluorescence* **2012**, *22*, 1189–1199.
- (150) Silva, N. J.; Machado, F. B.; Lischka, H.; Aquino, A. J. *Physical Chemistry Chemical Physics* **2016**, *18*, 22300–22310.
- (151) McCann, J. J.; Choi, U. B.; Zheng, L.; Weninger, K.; Bowen, M. E. *Biophysical journal* **2010**, *99*, 961–970.
- (152) Minton, A. P. *Journal of biological chemistry* **2001**, *276*, 10577–10580.
- (153) Israelachvili, J. N.; McGuiggan, P. M. *Science* **1988**, *241*, 795–800.
- (154) Kuznetsova, I. M.; Turoverov, K. K.; Uversky, V. N. *International journal of molecular sciences* **2014**, *15*, 23090–23140.
- (155) Nakano, S.-i.; Miyoshi, D.; Sugimoto, N. *Chemical reviews* **2014**, *114*, 2733–2758.
- (156) Nakano, S.-i.; Karimata, H.; Ohmichi, T.; Kawakami, J.; Sugimoto, N. *Journal of the American Chemical Society* **2004**, *126*, 14330–14331.

- (157) Miyoshi, D.; Sugimoto, N. *Biochimie* **2008**, *90*, 1040–1051.
- (158) Lüsse, S.; Arnold, K. *Macromolecules* **1996**, *29*, 4251–4257.
- (159) Banka, P.; Selser, J.; Wang, B.; Shenoy, D.; Martin, R. *Macromolecules* **1996**, *29*, 3956–3959.
- (160) Yoon, S. G.; Yang, Y.; Jin, H.; Lee, W. H.; Sohn, A.; Kim, S.-W.; Park, J.; Kim, Y. S. *Advanced Materials* **2019**, *31*, 1806268.
- (161) Belder, D.; Warnke, J. *Langmuir* **2001**, *17*, 4962–4966.
- (162) Fang, Y.; Giesecke, M.; Furo, I. *The Journal of Physical Chemistry B* **2017**, *121*, 2179–2188.
- (163) Okada, T. *Journal of Chromatography A* **1999**, *834*, 73–87.
- (164) Czyrko, J.; Sliwiak, J.; Imiolkzyk, B.; Gdaniec, Z.; Jaskolski, M.; Brzezinski, K. *Scientific reports* **2018**, *8*, 1–15.
- (165) Hu, Y.; Komoto, J.; Huang, Y.; Gomi, T.; Ogawa, H.; Takata, Y.; Fujioka, M.; Takusagawa, F. *Biochemistry* **1999**, *38*, 8323–8333.
- (166) Riordan, J. F. *Annals of Clinical & Laboratory Science* **1977**, *7*, 119–129.
- (167) Kilpin, K. J.; Dyson, P. J. *Chemical Science* **2013**, *4*, 1410–1419.
- (168) Winkler, K.; Paszewski, M.; Kalwarczyk, T.; Kalwarczyk, E.; Wojciechowski, T.; Gorecka, E.; Pociecha, D.; Holyst, R.; Fialkowski, M. *The Journal of Physical Chemistry C* **2011**, *115*, 19096–19103.
- (169) Harada, R.; Sugita, Y.; Feig, M. *Journal of the American Chemical Society* **2012**, *134*, 4842–4849.